



Chemical Heterogeneity of Mg, Mn, Na, S, and Sr in Benthic Foraminiferal Calcite

Inge van Dijk^{1*}, Aurélia Mouret¹, Marine Cotte^{2,3}, Sandrine Le Houedec¹, S. Oron^{4,5}, Gert-Jan Reichart^{6,7}, Juan Reyes-Herrera^{2,8}, Helena L. Filipsson⁹ and Christine Barras¹

¹ LPG UMR CNRS 6112, University of Angers, UFR Sciences, Angers, France, ² European Synchrotron Radiation Facility, Grenoble, France, ³ Sorbonne Universités, UPMC Univ Paris 06, CNRS, UMR 8220, Laboratoire d'Archéologie Moléculaire et Structurale (LAMS), Paris, France, ⁴ Department of Marine Geosciences, Charney School of Marine Sciences, University of Haifa, Haifa, Israel, ⁵ The Interuniversity Institute for Marine Sciences, Eilat, Israel, ⁶ Department of Ocean Systems, NIOZ-Royal Netherlands Institute for Sea Research and Utrecht University, Den Burg, Netherlands, ⁷ Faculty of Geosciences, Utrecht University, Utrecht, Netherlands, ⁸ Faculty of Agricultural Sciences, Autonomous University of Chihuahua, Chihuahua, Mexico, ⁹ Department of Geology, Lund University, Lund, Sweden

OPEN ACCESS

Edited by:

Aleksey Sadekov,
University of Western
Australia, Australia

Reviewed by:

Nina Keul,
University of Kiel, Germany
Takashi Toyofuku,
Japan Agency for Marine-Earth
Science and Technology, Japan

*Correspondence:

Inge van Dijk
inge.van.dijk@nioz.nl

Specialty section:

This article was submitted to
Biogeoscience,
a section of the journal
Frontiers in Earth Science

Received: 30 January 2019

Accepted: 17 October 2019

Published: 07 November 2019

Citation:

van Dijk I, Mouret A, Cotte M, Le
Houedec S, Oron S, Reichart G-J,
Reyes-Herrera J, Filipsson HL and
Barras C (2019) Chemical
Heterogeneity of Mg, Mn, Na, S, and
Sr in Benthic Foraminiferal Calcite.
Front. Earth Sci. 7:281.
doi: 10.3389/feart.2019.00281

The chemical composition of fossil foraminiferal shells (tests) is widely used as tracers for past ocean chemistry. It is, therefore, important to understand how different (trace) elements are transported and incorporated into these tests from adjacent seawater. The elemental distribution within the walls of foraminiferal tests might be used to differentiate between proposed transport mechanisms. Here, the microdistribution of Mg, Mn, Na, S, and Sr in tests of three species of foraminifera, known to have contrasting test chemistry, is investigated by a combination of electron probe microanalysis (EPMA) and nanoscale secondary ion mass spectrometry (nanoSIMS), micro-X-ray fluorescence (μ XRF), and micro-X-ray absorption near-edge structure (μ XANES) analyses. The three investigated species are the symbiont-barren *Ammonia* sp. T6 and *Bulimina marginata*, which precipitate a low-Mg calcite test, and the symbiont-bearing species *Amphistegina lessonii*, which produces a test with intermediate Mg content. Because all analyzed tests were formed under controlled and identical laboratory conditions, the observed distributions of elements are not due to environmental variability but are a direct consequence of the processes involved in calcification or, in the case of *A. lessonii*, possibly symbiont activity. Despite some variability in elemental microdistribution between specimens from a given species, our combined dataset shows species-specific distributions of the elements (e.g., peak heights and/or band-widths) and also a systematic collocation of Mg, Na, S, and Sr for all three species, suggesting a coupled or simultaneous uptake, transport, and incorporation of these elements during chamber addition. The observed trace element patterns generally reflect a laminar calcification model, suggesting that heterogeneity of these elements is intrinsically linked to chamber addition. Although the incorporation of redox-sensitive Mn depends on the Mn concentration of the culture medium, the Mn distribution observed in *Ammonia* sp. suggests that Mn transport is similarly linked to laminar calcification dynamics. However, for *B. marginata*, Mn banding was sometimes anticorrelated with Mg banding, suggesting that (bio)availability, uptake, and transport of Mn differ from those for

Ammonia sp. Our results from symbiont-bearing *A. lessonii* suggest that the activity of symbionts (i.e., photosynthesis/respiration) may influence the incorporation of Mn owing to alternation of the chemistry in the microenvironment of the foraminifera, an important consideration in the development of this potential proxy for past oxygenation of the oceans.

Keywords: benthic foraminifera, chemical heterogeneity, elemental banding, element incorporation, manganese, biomineralization

INTRODUCTION

The chemical composition of the carbonate shells (tests) of foraminifera, unicellular cosmopolitan protists, is widely used to reconstruct past ocean conditions (Lear et al., 2000; Hönisch and Hemming, 2005). Lately, the incorporation of redox-sensitive element manganese (Mn) has been studied as a potential proxy for paleo-oxygenation or sediment redox conditions (e.g., Reichart et al., 2003; Groeneveld and Filipsson, 2013; Koho et al., 2015; McKay et al., 2015; Groeneveld et al., 2018; Ní Fhlaithearta et al., 2018; Petersen et al., 2018; Guo et al., 2019). However, questions have been raised about the heterogeneity of Mn in the test wall for different species of foraminifera (Barras et al., 2018), which is crucial to know for the development and application of foraminiferal test Mn/Ca as an oxygenation proxy. Similarly, microscale variations in the magnesium (Mg) distribution, which are observed in all species, are hypothesized to be the cause of most of the Mg/Ca variability within and between specimens (Elderfield et al., 2002; Eggins et al., 2003; Sadekov et al., 2005). This potentially affects the reliability of Mg/Ca-based proxies (e.g., Nürnberg et al., 1996) used for reconstruction of paleo-temperatures (Sadekov et al., 2008) and habitat migration of planktonic foraminifera (Eggins et al., 2003). Investigating and understanding trace element distribution at the sub-micrometric scale in foraminiferal tests are, therefore, needed in order to fundamentally understand the processes involved and minimize the potential impact on paleo-environmental reconstructions.

Heterogeneity is a trait of biologically precipitated minerals (Allison et al., 2001; Freitas et al., 2009), including the calcium carbonate precipitated by foraminifera. This trace element variability has been explained by so-called vital effects, a term introduced by Urey et al. (1951), which covers varying factors and processes, including (i) ontogenetic-related changes or migration of foraminifera in the sediment or water column during their life cycle (e.g., Elderfield et al., 2002; Hintz et al., 2006) and (ii) processes involved in or active during biomineralization (Weiner and Dove, 2003), for instance, pH regulation during chamber formation (Toyofuku et al., 2017), or the presence of organic compounds (Kunioka et al., 2006; Mavromatis et al., 2017).

Over the last decade, there has been an increase in the use of high-resolution analysis techniques, such as laser ablation inductively coupled plasma mass spectrometry (LA-ICP-MS). This allowed for the measurement of single chambers of foraminiferal tests (Wu and Hillaire-Marcel, 1995; Reichart et al., 2003) and has been further developed to enable imaging (Evans and Müller, 2013) and depth profiling (Vetter et al.,

2013; Fehrenbacher et al., 2015) chemical variation within a single chamber wall. These methods are ideally used for larger foraminifera or foraminifera with a relatively thick test wall. Depth profiling is more complicated for most of the smaller foraminiferal species, because chamber walls are thin ($\sim 10 \mu\text{m}$) and generally also more curved, causing mixing of the elemental signal from different depths within the test. Other approaches exist for analyzing element distribution on microscale in foraminiferal calcite using non- (or less) destructive methods, including electron probe microanalysis (EPMA; Sadekov et al., 2005) or nanoscale secondary ion MS (nanoSIMS; Sano et al., 2005; Hoppe et al., 2013). In addition to the distribution of trace elements, the coordination and speciation of elements can be analyzed using micro-near-edge X-ray absorption fine structure (μNEXAFS) or micro-X-ray absorption near-edge structure (μXANES) (Reeder et al., 1999; Branson et al., 2013), providing information on the characteristic of element incorporation, and substitution in foraminiferal calcite and, therefore, calcification mechanisms.

Chemical variability, or so-called banding, of Mg/Ca in the chamber wall has been the most widely studied owing to the importance of Mg/Ca as a proxy for seawater temperature (Nürnberg et al., 1996). For planktic foraminifera, experiments show Mg variability being linked to day–night cycles (Eggins et al., 2004; Spero et al., 2015; Fehrenbacher et al., 2017) or crust formation (Eggins et al., 2003; Steinhardt et al., 2015). However, because a day–night Mg/Ca variation is observed for both symbiont-barren and symbiont-bearing species (for an overview, see Fehrenbacher et al., 2017), chemical heterogeneity in the test is not likely to be directly linked to symbiont activity. A chemical variation within test of benthic species has been studied less intensely (e.g., Erez, 2003; Branson et al., 2015; van Dijk et al., 2017b, 2019; Geerken et al., 2018) and is often attempted to be explained by processes involved in biomineralization, like transport of ions during calcification (Geerken et al., 2019) or changes in internal pH during calcification (Branson et al., 2015).

For the accuracy of the application of foraminiferal E/Ca ratios (where E represents a trace element) as proxies for past environmental conditions, it is important to deconvolute elemental heterogeneity caused by vital effects from the environmentally induced variability (e.g., Zeebe et al., 2008; Hathorne et al., 2009). To investigate the biological-induced trace element variability, it is necessary to study the elemental variability of foraminiferal calcite grown under controlled and geochemically stable conditions. Culture experiments in stable conditions also show banding of several elements, including Na

(Geerken et al., 2018, 2019) and S (Paris et al., 2014; van Dijk et al., 2017b). However, most of these studies so far focused on one (group of) species and/or one element of interest, as a function of changes in physical parameters such as salinity (Geerken et al., 2018), light-level (e.g., Fehrenbacher et al., 2017), or seawater chemistry (e.g., Paris et al., 2014). The distribution of multiple trace elements in foraminiferal tests has been studied less often but is recently receiving more and more attention (Geerken et al., 2019; Glock et al., 2019).

In this study, we present the microscale distribution of Mn and compare this to the distribution of Mg, Na, S, and Sr within the test wall of benthic foraminifera. We investigate test walls of three different species: symbiont-barren species *Ammonia* sp. and *Bulimina marginata* precipitating a low Mg test and symbiont-bearing species *Amphistegina lessonii*, which calcifies a test with intermediate Mg content. Studies focusing on *Amphistegina* and *Ammonia* are scarce (Erez, 2003; van Dijk et al., 2017b, 2019; Geerken et al., 2018) compared with studies on planktonic species, and this is the first time that element distribution within the tests walls of *B. marginata* is investigated. Previous research by LA-ICP-MS measurements on single chambers (Barras et al., 2018) showed contrasting ontogenetic trends in Mn/Ca between *Ammonia* sp. and *B. marginata*, which resulted in a model including Mn adsorption between calcite layers to explain these trends. In the present study, we aim to improve the spatial resolution of the analyses, and we study in detail the microdistribution of this element using EPMA and nanoSIMS, as well as the speciation of Mn by μ XANES to test this model. The nanoSIMS dataset complements the dataset obtained by EPMA, enabling us to extend our dataset to the lower culture treatment [Mn], and adds information on Sr distribution. By including species with and without symbionts, we, furthermore, examine whether symbiont activity in the microenvironment around the foraminifer (e.g., production of oxygen) influences incorporation of Mn. By including several other elements (Mg, Na, S, and Sr), it is possible to deconvolve vital effects that affect other elements from effects typical for Mn.

MATERIALS AND METHODS

Experimental Protocol

The specimens analyzed in this study have been cultured in controlled laboratory conditions with different manganese concentrations ($[Mn] = \sim 2, 10, 100$, and $600 \mu\text{mol/L}$). Specimens of *Ammonia* sp. T6 (identified following Richirt et al., 2019) and *Bulimina marginata* have been grown for 2 months in the experiments described in detail in Barras et al. (2018). Specimens of *Amphistegina lessonii* were cultured in the same system in slightly different conditions (mainly temperature and light) that are described below. Specimens of *A. lessonii* were collected at a depth of between 10 and 25 m by scuba diving in the Red Sea, near Eilat, on June 2016. Average temperature and salinity were, respectively, $\sim 24^\circ\text{C}$ and 40 at the time of collection. Samples were transported to the laboratory at the University of Angers (France), stored in artificial seawater (ASW, Red Sea Salt) with salinity of 35 laced with calcein (10

mg/L), and kept at laboratory temperature ($\sim 24^\circ\text{C}$). Calcein labeling prior to the experiment allows for the identification of chambers formed before the start of the experiment to distinguish chambers precipitated during the experiment (Bernhard et al., 2004). An Olympus SZX-164 stereomicroscope equipped with epifluorescence optics (excitation at 470 nm, emission at 500 nm) was used to observe calcein-labeled chambers. Specimens of *A. lessonii* were cultured, in the summer of 2016, in the same setup as described in Barras et al. (2018), that is, in four aquaria maintained in hypoxic conditions with different manganese concentrations ($[Mn] = \sim 2, 10, 100$, and $600 \mu\text{mol/L}$). However, to culture this tropical species, a day-night cycle was set up (12 h/12 h, light intensity $\sim 10 \mu\text{Einstein}$), and the temperature was set at 25°C . The lower temperature used in the previous experiment ($T = 12^\circ\text{C}$; Barras et al., 2018) might have decreased symbiont activity (Fujita et al., 2014) and probably reduced calcification. After calcein pre-staining, specimens of both species were added in open vials (50 ml) that were introduced in the aquaria. To each vial, 100 μl of frozen *Phaeodactylum tricornutum* (48.6 mg/L) was added.

Four aquaria were filled with 10 L of ASW (Red Sea Salt) with salinity of ~ 35 . In three aquaria, Mn was enriched by adding $\text{MnCl}_2 \cdot 2\text{H}_2\text{O}$ (Merck), resulting in four conditions with different [Mn]: Aq0 $\sim 2 \mu\text{mol/L}$ (corresponding to natural concentration of Mn in Red Sea Salt), Aq10 $\sim 10 \mu\text{mol/L}$, Aq100 $\sim 100 \mu\text{mol/L}$, and Aq600 $\sim 600 \mu\text{mol/L}$. The highest [Mn] corresponds to pore water [Mn] from coastal Mn-rich environments (Sulu-Gambari et al., 2016; Barras et al., 2018). To maintain stable [Mn] during the duration of the experiment, all four aquaria were kept at hypoxic conditions by continuous bubbling with a mixture of N_2/CO_2 (0.04%) gas, and oxygen concentration was continuously monitored with four micro-optodes (Unisense). For the duration of the experiment, the average dissolved oxygen saturation was $35 \pm 3\%$ (standard deviation [SD]) for Aq0, $29 \pm 5\%$ for Aq10, $30 \pm 3\%$ for Aq100, and $32 \pm 3\%$ for Aq600. Beside oxygen saturation, several physico-chemical parameters were monitored weekly, including salinity, pH, and total alkalinity (Table 1).

All four aquaria were sampled daily to measure elemental composition of the seawater. Concentrations of Ca, Mg, Mn, Na, and Sr were measured by ICP atomic emission spectroscopy (ICP-AES, Thermo Scientific iCAP 6300 Radial), and results are presented in Table 1. Mn/Ca_{SEAWATER} was stable over the experiment, with concentrations of 0.30 ± 0.13 , 1.09 ± 0.03 , 9.76 ± 0.59 , and $50.89 \pm 0.78 \text{ mmol/mol}$ for Aq0, Aq10, Aq100, and Aq600, respectively. Values are very similar to those of the experimental setup of Barras et al. (2018). Average element-to-calcium ratios were $4.86 \pm 0.09 \text{ mol/mol}$ for Mg/Ca_{SEAWATER}, $45.67 \pm 0.61 \text{ mol/mol}$ for Na/Ca_{SEAWATER}, and $11.77 \pm 0.15 \text{ mmol/mol}$ for Sr/Ca_{SEAWATER}. The chemical composition of the culture media is very similar to that of Barras et al. (2018): $4.87 \pm 0.05 \text{ mol/mol}$ for Mg/Ca_{SEAWATER}, $45.44 \pm 0.51 \text{ mol/mol}$ for Na/Ca_{SEAWATER}, and $11.41 \pm 0.11 \text{ mmol/mol}$ for Sr/Ca_{SEAWATER}.

The duration of the experiment with tropical foraminifera was 17 days, in which foraminifera grew one to five new chambers. After the experiment, foraminifera were cleaned with 5% NaOCl

TABLE 1 | Culture parameters from the four different treatments (Aq0, Aq10, Aq100, and Aq600) used in the experiment.

Parameter	Aq0	Aq10	Aq100	Aq600
O ₂ sat (% ± SD)	35 ± 3	29 ± 5	30 ± 3	32 ± 3
Salinity	35.9 ± 0.6	35.8 ± 0.5	35.9 ± 0.4	35.9 ± 0.4
Total alkalinity (mmol/L ± SD)	2,132 ± 2	2,130 ± 2	2,088 ± 2	2,078 ± 2
pH (Avg. ± SD)	7.98 ± 0.04	7.93 ± 0.05	8.00 ± 0.02	8.00 ± 0.01
Ca (mM)	10.6 ± 0.1	10.5 ± 0.2	10.2 ± 0.1	10.2 ± 0.1
Mg (mM)	51.1 ± 0.5	50.3 ± 0.8	50.8 ± 0.7	49.9 ± 0.7
Mn (μM)	3.1 ± 1.4	11.5 ± 0.4	99.7 ± 6.2	517.6 ± 10.5
Na (mM)	483.6 ± 5.5	474.4 ± 8.1	468.4 ± 5.5	471.9 ± 7.6
Sr (μM)	123.8 ± 1.4	122.9 ± 1.9	121.1 ± 1.1	121.5 ± 1.0
Mg/Ca (mol/mol)	4.80 ± 0.01	4.77 ± 0.02	4.98 ± 0.05	4.91 ± 0.03
Mn/Ca (mmol/mol)	0.30 ± 0.13	1.09 ± 0.03	9.76 ± 0.59	50.89 ± 0.78
Na/Ca (mol/mol)	45.44 ± 0.39	44.97 ± 0.21	45.86 ± 0.24	46.40 ± 0.39
Sr/Ca (mmol/mol)	11.64 ± 0.08	11.65 ± 0.04	11.86 ± 0.05	11.94 ± 0.08

Average value (±SD) of physiochemical parameters of the culture media; oxygen saturation, salinity ($n = 3$), total alkalinity ($n = 3$), and pH ($n = 4$). Average elemental composition and E/Ca values (±SD) of the artificial seawater, measured by inductively coupled plasma atomic emission spectroscopy (ICP-AES).

for a minimum of 1 h until the tests were bleached. After being rinsed three times with de-ionized water, specimens were oven-dried (45°C) and stored until measurements.

Elemental Microdistribution in Foraminiferal Tests

Electron Probe Microanalysis

Specimens of *A. lessonii* from the experiment described in this study, together with specimens of *Ammonia* sp. and *B. marginata* from the study of Barras et al. (2018), were measured on a field emission EPMA (JEOL JXA-8530F) at Utrecht University (the Netherlands) to investigate the intra-test incorporation of Mg, S, Na, and Mn. Specimens of each species from all of the four culture conditions (Aq0, Aq10, Aq100, and Aq600) were embedded under vacuum in resin (2020 Araldite® resin by Huntsman International LLC) using 2.5-cm epoxy plugs. Samples were polished using increasingly finer sanding paper, resulting in exposure of cross section of chamber walls. In the final polishing step, a diamond emulsion with grains of 0.04 μm was used to create a smooth surface. Scanning electron microscope (SEM) images were taken with a tabletop Hitachi TM3000 at the Royal Netherlands Institute for Sea Research (the Netherlands) to find areas of interest (Figure 1).

After the carbon coating, the samples were placed in the microprobe sample holder. After selection of target areas, several small high-resolution maps (130 × 97 pixels, pixel size was generally 0.2 μm) were analyzed at 12.0 kV in beam scan mode with a dwell time of 350 ms, providing elemental maps for Ca, Mn, Mg, S, and Na. Part of the data obtained for Mg and S have previously been published (van Dijk et al., 2019), but the dataset is extended by including more maps and will be used for

comparison with Mn and Na distribution. All EPMA data were further processed in MATLAB following a protocol described in van Dijk et al. (2019). In short, resin, pores, and edge areas were excluded from the final maps by excluding areas where Ca levels were <10,000 counts (Figure 2C). The resulting concentration (level) maps were converted to semiquantitative element-to-calcium maps (E/Ca) by applying a calibration based on mineral standards. We used diopside (CaMgSi₂O₆) for Ca, forsterite (Mg₂SiO₄) for Mg, jadeite (NaAlSi₂O₆) for Na, celestine (SrSO₄) for S, and tephroite (Mn₂SiO₄) for Mn. Resulting matrices of Mg, S, Na, and Mn were divided with the Ca matrix, to allow for a semiquantification of the counts to concentrations to obtain E/Ca (mmol/mol) maps. We choose to report these ratios as E/Ca_{EPMA} to clearly distinguish these data from quantitative data obtained by other methods, for example, LA-ICP-MS. For all maps, distribution profiles were created by selecting rectangular areas perpendicular to the chamber wall, so-called transect maps, after rotation of the total matrix (Figure 2D). Resin and pore areas were, as mentioned above, also excluded for the calculation of profiles. For every element, we calculated average E/Ca_{EPMA} per column of the transect maps to create an E/Ca_{EPMA} distribution profile, which was plotted and compared with the distribution profile of Mg/Ca_{EPMA} (Figure 3). Using the coefficient of determination (R^2) and the slope of the relation, we assess whether element distributions of S, Na, and Mn are (positively or negatively) significantly correlated with the Mg distribution.

Distribution profiles of the transect maps were used to localize peak and base areas and determine peak value (maximum value within band area, E/Ca_{MAX}) and the sequential base value (minimum value within non-band area, E/Ca_{MIN}) of each element, of the primary and any secondary peaks, counted from interior to exterior (for a more detailed description, see Figure 2 in van Dijk et al., 2019). For S/Ca_{EPMA} and Na/Ca_{EPMA}, which have maximum values close to the high intensity band of Mg/Ca_{EPMA}, we calculated maximum and minimum E/Ca_{EPMA} values at the location of the Mg/Ca_{EPMA} peak and base, respectively. This allows us to examine the difference of peak and/or base intensity within one chamber wall and between species for Mg/Ca_{EPMA}, S/Ca_{EPMA}, and Na/Ca_{EPMA} and investigate the link in the microdistribution of these elements. Mn/Ca_{EPMA} was often not correlated to the highly concentrated band of Mg/Ca_{EPMA}, so we calculated the maximum and minimum transect values independently from the location of the Mg band. We express the peak intensity as “peak factor,” which is the peak value divided by the associated base value (E/Ca_{MAX}/E/Ca_{MIN}). After testing for variance with an *F*-test, we performed bilateral unpaired *t*-tests to determine if values of primary and secondary peaks (PI/PII) and bases (BI/BII), as well as peaks and bases (PI/BI or PII/BII), are significantly ($p < 0.05$) different. We also indicate which *p*-values are significant after Bonferroni correction, which corrects for type I errors (while underestimating for type II errors), leading to a more conservative critical value. This (more conservative) critical value ($p_{\text{Bonferroni}}$) is determined by $p < 0.05/n$, in which n is the total number of *t*-test used. For our study, $p_{\text{Bonferroni}} < 0.00086$.

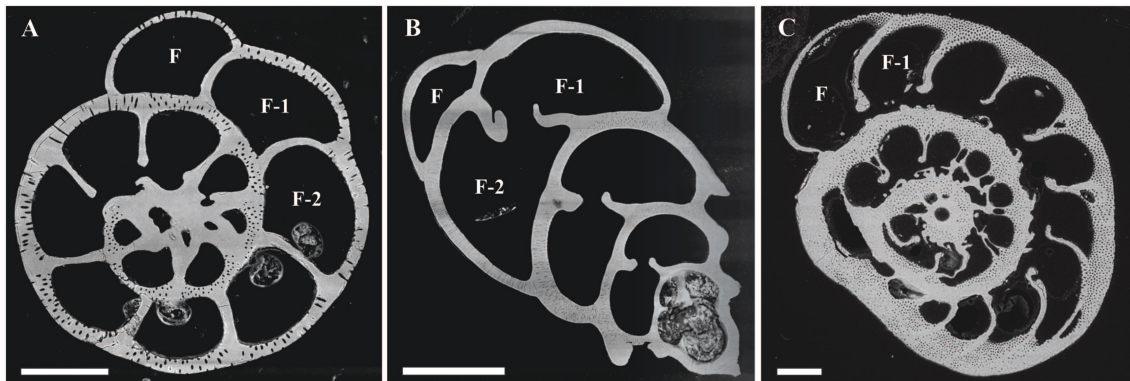


FIGURE 1 | Examples of SEM images of polished specimens of (A) *Ammonia* sp. T6 (B), *Bulimina marginata*, and (C) *Amphistegina lessonii*. Chambers precipitated during the experiment are recognized owing to pre-staining (see Experimental Protocol section) and are numbered from final (F) to older chambers (e.g., F-1 and F-2). Scale bar is 100 μ m. SEM, scanning electron microscope.

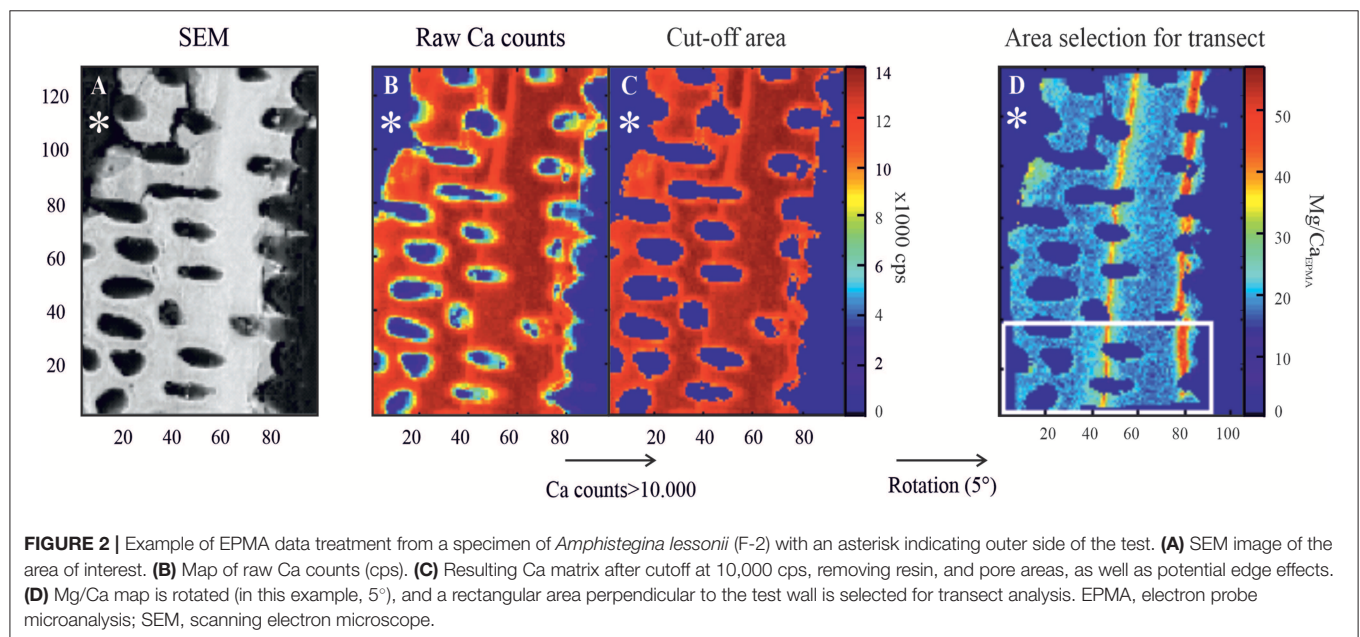
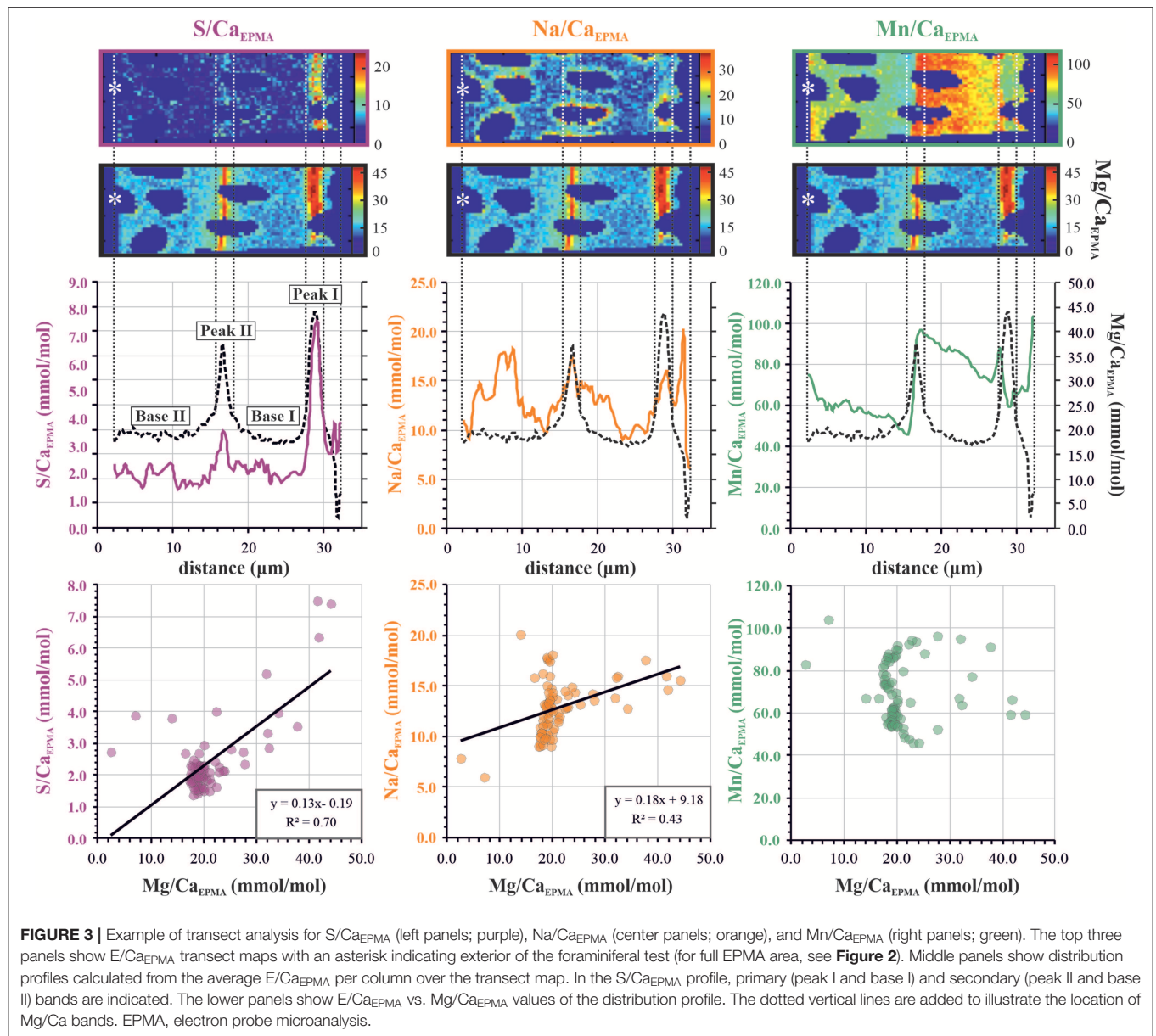


FIGURE 2 | Example of EPMA data treatment from a specimen of *Amphistegina lessonii* (F-2) with an asterisk indicating outer side of the test. (A) SEM image of the area of interest. (B) Map of raw Ca counts (cps). (C) Resulting Ca matrix after cutoff at 10,000 cps, removing resin, and pore areas, as well as potential edge effects. (D) Mg/Ca map is rotated (in this example, 5°), and a rectangular area perpendicular to the test wall is selected for transect analysis. EPMA, electron probe microanalysis; SEM, scanning electron microscope.

Nanoscale Secondary Ion Mass Spectrometry Analyses

To investigate the distribution of Mn in the different species from aquaria with the lowest seawater [Mn], we selected several specimens of *Ammonia* sp., *B. marginata*, and *A. lessonii* for a nanoSIMS analysis. NanoSIMS has a lower detection limit and better spatial resolution than has EPMA and, therefore, may show if high-Mn absorption layers are present in the test wall, as hypothesized by Barras et al. (2018). Specimens were embedded in resin (EpoFix by Struers) in aluminum rings with a diameter of 1 cm. Samples were dried under vacuum at room temperature overnight, which allowed for a gentle degassing of the samples. Samples were polished using increasingly finer polishing paper, from 30 to 0.3 μ m, resulting in a smooth exposure of cross section of chamber walls. SEM images were taken at SCIAM platform

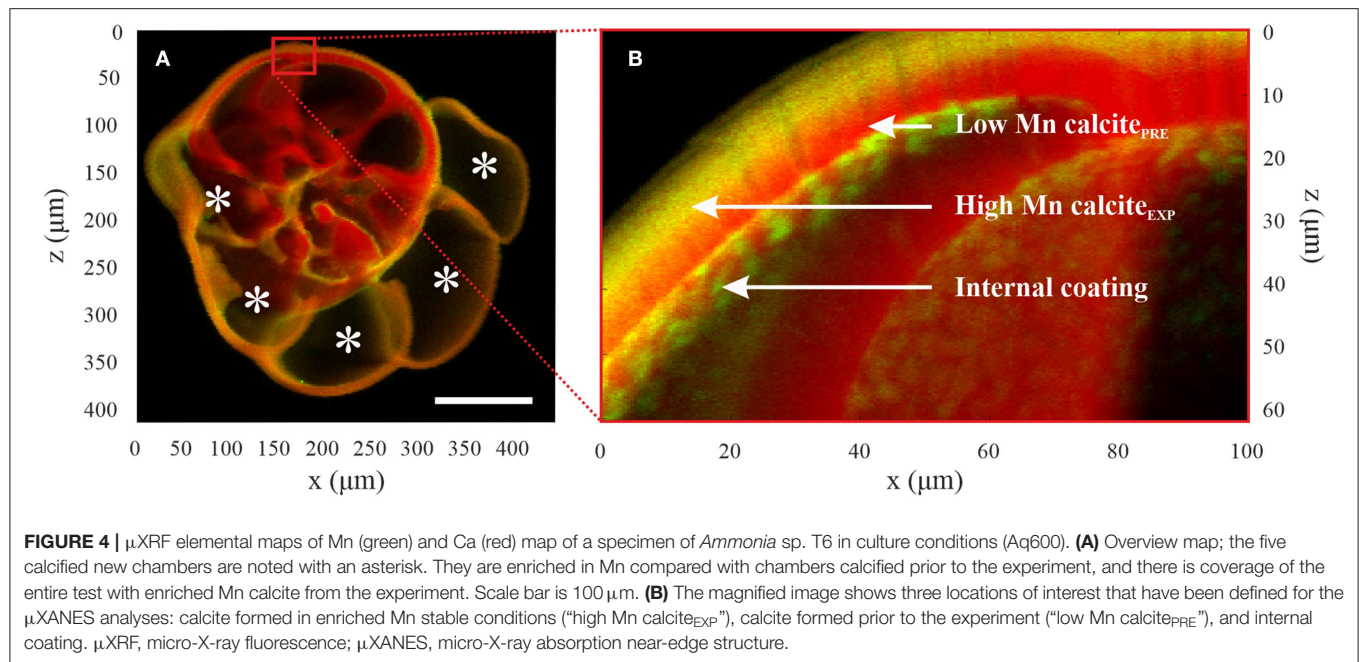
at the University of Angers (France) to assert the quality of the polishing and identify areas of interest. The samples were coated with a 15-nm gold layer to prevent buildup of a charge on the surface during the nanoSIMS analyses. A primary beam of O^- , focused to a spot size of about 450 nm (full width at half maximum [FWHM]) permitted extraction of $^{40}Ca^+$, $^{45}Ca^+$, $^{24}Mg^+$, $^{55}Mn^+$, $^{86}Sr^+$, and $^{88}Sr^+$ ions, which were counted in parallel in electron multipliers. In the imaging mode, selected areas (usually $25 \times 25 \mu m$) were first implanted in order to clean up the surface. The area was then imaged by scanning a smaller beam (~ 450 nm, 26 pA) with a resolution of 256×256 pixels and a dwell time of 5 μs /pixel. Typically, 40 layers of data acquisition were collected and accumulated (after drift correction) into one set of individual isotopic images using the L'IMAGE[®] software (developed by Dr. Larry Nittler, Carnegie



Institution of Washington DC, USA). In addition, specific areas of interest were selected for horizontal or vertical linescans with higher spatial resolution. In this case, pre-sputtering was first performed to clean up the surface (two linescans with a dwell time of 2 s/pixel and 56 pA for the O^- beam; spot size of around $1\ \mu\text{m}$). The data acquisition was performed in the same track with a primary beam focused to about 400 nm (10 scans with 2 s/pixel). The accumulated Mg/Ca , Mn/Ca , and Sr/Ca ratios from these linescans were normalized to a range between 0 and 1 in order to facilitate comparison of peak positions. Absolute concentration ratios were not obtained. Applying the same method as for the EPMA data, we obtained peak and base values, which could be compared using bilateral unpaired t -tests (significance level: 95%).

Micro-X-Ray Fluorescence and Micro-X-Ray Absorption Near-Edge Structure Analyses

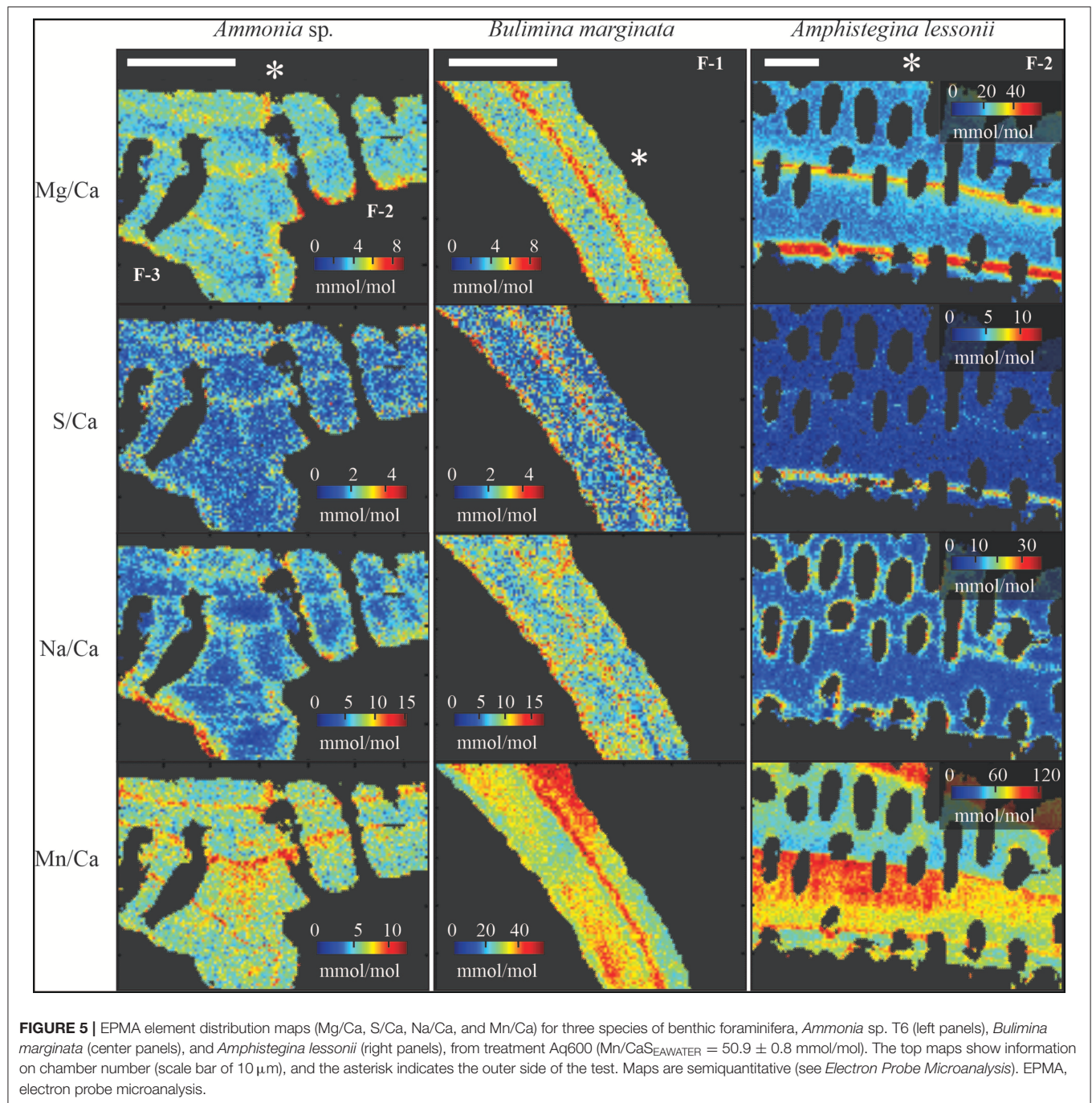
To investigate the Mn speciation in tests of *Ammonia* sp. and *B. marginata* cultured in different $[Mn]$, we performed μXRF and μXANES analyses at the Mn K-edge. These analyses were performed with the scanning X-ray microscope (SXM) end-station hosted at the X-ray microscopy beamline ID21 of the European Synchrotron Radiation Facility (ESRF) in Grenoble (France; Cotte et al., 2017). Analyses were performed on samples of Aq100 and Aq600 prepared for EPMA (see *Electron Probe Microanalysis* for embedding and polishing details). Samples were mounted vertically, with an angle of XRF 62° with respect to the incident beam. X-rays were generated using an undulator in which gap was adjusted synchronously with the fixed exit



double-crystal Si (111) monochromator (DCM) Bragg angle. The DCM energy calibration was performed using a Mn foil (maximum of the derivative of XANES spectrum set at 6.5392 keV). The incident beam was focused with Kirkpatrick–Baez mirrors down to a probe of $0.6 \times 0.3 \mu\text{m}^2$ ($h \times v$). XRF signals were collected in the horizontal plane and at 69° with respect to the incident beam direction by means of an 80-mm^2 single energy-dispersive silicon drift detector from SGX (25 μm Be window). Elemental maps were obtained by exciting XRF employing a monochromatic primary beam of 6.64 keV while raster scanning the samples over two-dimensional (2D) regions (100 ms/pixel). The software PyMca (Solé et al., 2007; Cotte et al., 2016) was used to batch-fit the XRF spectra and to separate the contribution of the different elements. Low-resolution maps were first acquired over the entire test with a 1–2- μm step (Figure 4A). On these overview maps, high-resolution maps were acquired with a 0.2–0.5- μm step to identify the main regions of interest (Figure 4B): calcite with high [Mn] formed in the experimental conditions ("high Mn calcite_{EXP}"), calcite formed prior to the experiments with low [Mn] relative to the chambers calcified in culture ("low Mn calcite_{PRE}"), calcite formed prior to the experiments with high [Mn] relative to the chambers calcified in culture ("high Mn calcite_{PRE}"; note that this is only the case for one specimen of *B. marginata*), and the internal coating found on the internal side of the test that exhibits a high [Mn] and which has a patchy distribution. When present, this internal coating was showing high concentration of Mn in the pores of the test.

On these detailed maps (Figure 4B), μ XANES spectra were acquired at the points of interest in XRF mode by scanning the primary energy at the Mn K-edge (6.52–6.64 keV; energy step: 0.4 eV). Spectra normalization was performed using PyMca software. To identify if Mn shows the same coordination depending on different parameters [i.e., species, [Mn] in the seawater of the aquaria, and locations of interest in the

sample], a statistical analysis of spectra was performed using the Orange open-source software (Demšar et al., 2013; Toplak et al., 2017). Each spectrum was labeled by the name of species (*Ammonia* or *Bulimina*), the culture media conditions (Aq100 or Aq600), and the location of the spectrum in the test structure, as determined from the μ XRF maps of Ca and Mn (i.e., "high Mn calcite_{EXP}", "low Mn calcite_{PRE}", "high Mn calcite_{PRE}", and "internal coating"). A set of references was also included in the dataset. Some of the references were acquired during the same session at ID21, that is, references Mn metal and MnO₂, MnO(OH), Mn₃O₄, MnCl₂, and MnSO₄, prepared as powder spread in a tape (spectra simultaneously acquired in transmission and XRF modes). Other reference spectra were kindly provided by Dr. Samuel M. Webb (SLAC) [manganoan calcite ((Ca,Mn)CO₃), kutnohorite (CaMn(CO₃)₂), rhodochrosite (MnCO₃), and KMnO₄], calibration tuned using a MnCO₃ reference) previously published in Johnson et al. (2016) and by Peter Kopittke (MnSO₄, MnPO₄, MnCO₃, Mn(II) oxide (MnO), Mn(III) oxide (Mn₂O₃), Mn(IV) oxide (MnO₂), pyrolusite (MnO₂), hausmannite (Mn₃O₄), Mn-oxalate, Mn-citrate, Mn-cystine, Mn-malate, and Mn-phytate, calibration tuned using the Mn reference) previously published in Blamey et al. (2018). The ATHENA software (Ravel and Newville, 2005) was used for interpolation and energy shifting on the external references. Further data processing consisted in the calculation of the second derivative over normalized spectra, using the Savitzky–Golay method. The second derivative was used to remove constant and linear components that could be introduced by possible discrepancy on normalization between data and references sets. Furthermore, a principal component analysis (PCA) was applied to the different datasets to compare the coordination of Mn for the two species and between different points of interest. By comparing the spectra obtained from foraminiferal calcite with spectra of references material, in



particular the position of the edge and the white line peak (i.e., position of maximum absorption), we can investigate in which form Mn is present in the foraminiferal test.

RESULTS

Distribution of Mn, Mg, S, and Na by Electron Probe Microanalysis

Examples of element to calcium maps per species are presented in **Figure 5**. All three species show characteristic banding patterns

and peak intensities, depending on the element of interest. The most pronounced banding can be found in Mg/Ca and Mn/Ca maps, depending in the latter case of the seawater [Mn] of the culture experiment; that is, Mn banding is most visible for Aq100 and Aq600 and not in Aq10, owing to the limit of detection. *Ammonia* sp. shows thin bands of 1–2 μm of high E/Ca for Mg, S, Na, and Mn. Distributions of Mg, S, and Na follow the same pattern of thin bands in specimens of *Bulimina marginata* (1–3 μm) and *Amphistegina lessonii* (2–4 μm), but Mn/Ca distribution differs (**Figure 5**). For *B. marginata*, Mn/Ca

TABLE 2 | Average E/Ca (mmol/mol \pm SD) per species per treatment of total distribution maps EPMA.

Species	Aq	n	Mg/Ca _{EPMA} (mmol/mol)	Na/Ca _{EPMA} (mmol/mol)	S/Ca _{EPMA} (mmol/mol)	Mn/Ca _{EPMA} (mmol/mol)
<i>Ammonia</i> sp.	Aq10	3	4.0 \pm 0.2	5.2 \pm 0.4	1.6 \pm 0.2	n.d.
	Aq100	3	3.7 \pm 0.1	5.4 \pm 0.3	1.7 \pm 0.1	3.1 \pm 0.2
	Aq600	5	4.1 \pm 0.1	6.0 \pm 0.4	1.8 \pm 0.1	5.5 \pm 1.1
	All data	11	4.0 \pm 0.2	5.7 \pm 0.5	1.7 \pm 0.1	4.3 \pm 1.5
<i>Bulimina marginata</i>	Aq10	5	5.7 \pm 0.7	6.0 \pm 1.6	1.8 \pm 0.4	3.3 \pm 0.1
	Aq100	5	5.5 \pm 0.3	6.8 \pm 1.2	1.7 \pm 0.2	9.3 \pm 1.0
	Aq600	3	4.6 \pm 0.6	8.6 \pm 1.2	1.8 \pm 0.3	33.3 \pm 4.3
	All data	13	5.1 \pm 0.6	6.7 \pm 3.2	1.6 \pm 0.8	13.8 \pm 10.5
<i>Amphistegina lessonii</i>	Aq10	5	27.1 \pm 0.8	9.0 \pm 1.7	2.1 \pm 0.1	3.3 \pm 0.1
	Aq100	1	26.0 \pm 0.7	8.4 \pm 0.5	2.6 \pm 0.4	13.6 \pm 2.2
	Aq600	4	22.8 \pm 0.9	9.1 \pm 2.6	2.3 \pm 0.2	65.7 \pm 15.5
	All data	10	24.7 \pm 2.1	8.9 \pm 1.8	2.3 \pm 0.3	37.1 \pm 32.5

Ammonia sp. T6, total n = 10; *Bulimina marginata*, total n = 13; *Amphistegina lessonii*, total n = 8. The high SD of Mn/Ca_{EPMA} is due to the different seawater [Mn] of the aquaria. Mn counts were below detection limit. n.d., not detectable; EPMA, electron probe microanalysis.

is present as a thin highly concentrated band located close to the Mg band but is often heterogeneously distributed within the lamella. In contrast, for *A. lessonii*, Mn/Ca distribution is characterized by broad bands with either high or low Mn/Ca, corresponding to different lamella of the test wall.

We calculated average E/Ca_{EPMA} of all distribution maps obtained by EPMA (for examples, see **Figure 5** and **Supplementary Figures 1–3**) per species per culture treatment (i.e., Aq10, Aq100, and Aq600) (**Table 2**). Mg/Ca_{EPMA} and Na/Ca_{EPMA} are the lowest for *Ammonia* sp., 4.0 \pm 0.2 and 5.7 \pm 0.5 mmol/mol, respectively, and *B. marginata*, 5.1 \pm 0.6 and 6.7 \pm 3.2 mmol/mol, respectively, than are those of the larger benthic species *A. lessonii*, which has higher incorporation of Mg and Na, leading to Mg/Ca_{EPMA} and Na/Ca_{EPMA} of 24.7 \pm 2.1 and 8.9 \pm 1.8 mmol/mol, respectively. For these two element ratios, the differences between species are significant ($p < 0.05$), except for Na/Ca between *Ammonia* sp. and *B. marginata*. S/Ca_{EPMA} is not significantly different for the small benthic species, 1.7 \pm 0.1 and 1.6 \pm 0.8 mmol/mol for *Ammonia* sp. and *B. marginata*, respectively, whereas *A. lessonii* has significantly ($p < 0.05$) higher values on average, 2.3 \pm 0.3 mmol/mol. For a given [Mn] in seawater, Mn/Ca_{EPMA} increases from *Ammonia* sp. to *B. marginata* to *A. lessonii*, showing the highest incorporation of Mn in the latter species.

Mg, Na, and S Distribution: Electron Probe Microanalysis Peak Analysis

We analyzed 11, 8, and 10 EPMA transect maps of six, six, and nine specimens of *Ammonia* sp., *B. marginata*, and *A. lessonii*, respectively. The patterns observed in the microdistribution of Mg, Na, and S were comparable between specimens of a given species. Because seawater chemistry of these elements is stable in the experiment, we combined the data from all culture treatments (Aq10, Aq100, and Aq600), unlike [Mn], and calculated the average E/Ca_{EPMA}, which is presented as average peak and base values of the primary and secondary bands in **Figure 6** and

Table 3. For *Ammonia* sp. (11 primary bands and five secondary bands) and *A. lessonii* (10 primary bands and two secondary bands), we acquired enough secondary bands to investigate sequential peak and base values. In most cases, peak and base (e.g., PI/BI and PII/BII) and primary and secondary peak (PI/PII) values are significantly different ($p < 0.05$; **Table 4**). This is most obvious for Mg/Ca_{EPMA} (**Figure 6A**). Primary base and secondary base are, with the exception of Na/Ca in *A. lessonii*, always similar ($p > 0.05$; **Table 4**). Peaks are in general lower and less pronounced for the small benthic species, *Ammonia* sp. and *B. marginata* (peak factor of 1–2) compared with the large benthic species *A. lessonii* (peak factor of 1–4; **Table 3**).

When comparing the three species with each other, we observe that peak and base values of Mg/Ca (**Figure 6A**), Na/Ca (**Figure 6B**), and S/Ca (**Figure 6C**) are often significantly different ($p < 0.05$). When PI and BI are compared, Mg/Ca peaks (**Figure 6A**) are significantly different between all three species, whereas base values are different between the small benthic species (*Ammonia* sp. and *B. marginata*) compared with *A. lessonii*. For Na/Ca (**Figure 6B**), peak values are higher in *A. lessonii* compared with the small benthic species, whereas base values are significantly different between all three species. S/Ca peaks and bases (**Figure 6C**) are similar ($p > 0.05$) between *Ammonia* sp. and *B. marginata* but significantly different when comparing these species with *A. lessonii*.

Mn Distribution Patterns Obtained by Electron Probe Microanalysis

The distribution pattern of Mn/Ca_{EPMA} in the test wall is different for each of the species investigated, as it can be seen in EPMA maps presented in **Figure 5**, as well as the **Supplementary Information** (*Ammonia* sp., **Supplementary Figure 1**; *B. marginata*, **Supplementary Figure 2**; *A. lessonii*, **Supplementary Figure 3**). In species *Ammonia* sp., spatial distribution of Mn is linked to a Mg/Ca variation. In contrast, for the species *B. marginata*

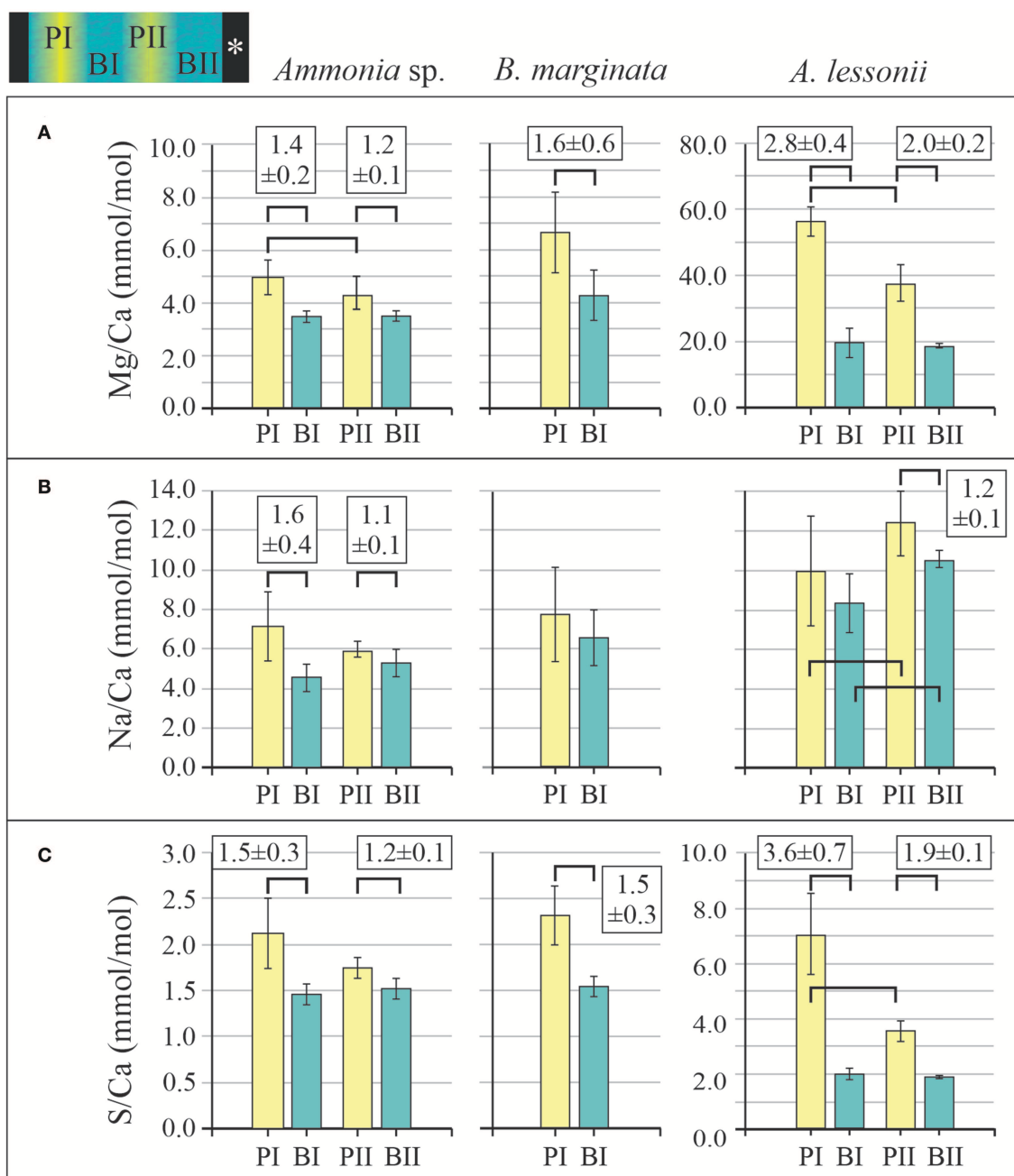


FIGURE 6 | EPMA average peak (E/Ca_{MAX} ; yellow) and base (E/Ca_{MIN} ; blue) values of primary peak and base (PI and BI) and secondary peak and base (PII and BII) for the three species *Ammonia* sp. T6 (left panels), *Bulimina marginata* (middle panels), and *Amphistegina lessonii* (right panels) for Mg/Ca_{EPMA} (A), Na/Ca_{EPMA} (B), and S/Ca_{EPMA} (C). Significant differences ($p < 0.05$) between peak and base values (e.g., PI and BI) are indicated with black brackets, and for these values, peak factors \pm SD ($E/Ca_{MAX}/E/Ca_{MIN}$) are given (see also Table 3). For calculation of peak and base values, see paragraph 2.3.1. The top shows a hypothetical transect map with locations of PI, BI, PII, and BII, with the asterisk indicating the outer part of the test. Note that the scale of the y-axis is different for *A. lessonii*, except for Na/Ca. EPMA, electron probe microanalysis.

and *A. lessonii*, the Mn/Ca_{EPMA} distribution is not strongly correlated or even sometimes anticorrelated to Mg/Ca_{EPMA} (see, e.g., Supplementary Figure 2B for *B. marginata* and Supplementary Figures 3A,C for *A. lessonii*). As explained in the Materials and Methods section, we, therefore, performed the

peak analysis again, focusing on Mn to obtain the minimum and maximum values per transect. For all three species, average peak and base values for Mn/Ca are presented in Figure 7. Average Mn/Ca_{EPMA} increases from Aq10 to Aq600, corresponding to higher incorporation of Mn with increasing

TABLE 3 | EPMA average values (see **Table 2**) and E/Ca_{MAX} and E/Ca_{MIX} values in mmol/mol for *Ammonia* sp. T6, *Bulimina marginata*, and *Amphistegina lessonii* with peak factor (PF; significant values, $p < 0.05$, in bold, see **Table 4**).

E/Ca	Species	Avg E/Ca _{EPMA} (mmol/mol)	Peak I E/Ca _{MAX} (mmol/mol)	Base I E/Ca _{MIN} (mmol/mol)	PF I	Peak II E/Ca _{MAX} (mmol/mol)	Base II E/Ca _{MIN} (mmol/mol)	PF II
Mg/Ca	<i>Ammonia</i> sp.	4.0 ± 0.2	4.9 ± 0.7	3.5 ± 0.2	1.4 ± 0.2	4.3 ± 0.2	3.5 ± 0.2	1.2 ± 0.1
	<i>Bulimina marginata</i>	5.1 ± 0.6	6.4 ± 1.5	4.2 ± 0.9	1.6 ± 0.6	n.m.	n.m.	n.m.
	<i>Amphistegina lessonii</i>	24.7 ± 2.1	56.6 ± 10.2	20.2 ± 4.3	2.8 ± 0.4	37.8 ± 5.6	19.1 ± 0.3	2.0 ± 0.2
Na/Ca	<i>Ammonia</i> sp.	5.7 ± 0.5	7.2 ± 1.7	4.6 ± 0.7	1.6 ± 0.4	5.9 ± 0.2	5.3 ± 0.6	1.1 ± 0.1
	<i>B. marginata</i>	6.7 ± 3.2	7.8 ± 2.4	6.6 ± 1.4	1.2 ± 0.2	n.m.	n.m.	n.m.
	<i>A. lessonii</i>	8.9 ± 1.8	10.0 ± 2.8	8.3 ± 1.6	1.2 ± 0.2	12.5 ± 2.1	10.6 ± 0.3	1.2 ± 0.1
S/Ca	<i>Ammonia</i> sp.	1.7 ± 0.1	2.1 ± 0.4	1.5 ± 0.1	1.5 ± 0.3	1.8 ± 0.1	1.6 ± 0.1	1.2 ± 0.1
	<i>B. marginata</i>	1.6 ± 0.8	2.3 ± 0.3	1.5 ± 0.1	1.5 ± 0.3	n.m.	n.m.	n.m.
	<i>A. lessonii</i>	2.3 ± 0.3	6.9 ± 1.4	1.9 ± 0.2	3.6 ± 0.7	3.5 ± 0.4	1.9 ± 0.2	1.9 ± 0.1

Locations for E/Ca_{MIN} and E/Ca_{MAX} are based on the peak and base location of Mg/Ca. *Ammonia* sp. $n = 11$ (I) and 5 (II), *B. marginata* $n = 8$ (I), and *A. lessonii* $n = 10$ (I) and 2 (II). n.m., not measured; EPMA, electron probe microanalysis.

TABLE 4 | Two-tailed p -values of unpaired t -test of comparison of means of primary and secondary peak (PI and PII) and base (BI and BII) values of E/Ca acquired by EPMA.

Species	Aq	E/Ca	PI/BI	PII/BII	PI/PII	BI/BII
<i>Ammonia</i> sp.	All	Mg/Ca	<u><0.0001</u>	<u><0.0001</u>	0.0091	0.9007
	All	S/Ca	<u><0.0001</u>	0.0009	0.0157	0.0997
	All	Na/Ca	0.002	0.0305	0.0168	0.0145
	Aq100	Mn/Ca	0.0011	n.a.	n.a.	n.a.
	Aq600	Mn/Ca	0.0062	n.a.	n.a.	n.a.
<i>B. marginata</i>	All	Mg/Ca	0.0023	n.a.	n.a.	n.a.
	All	S/Ca	<u><0.0001</u>	n.a.	n.a.	n.a.
	All	Na/Ca	0.2429	n.a.	n.a.	n.a.
	Aq10	Mn/Ca	0.3118	n.a.	n.a.	n.a.
	Aq100	Mn/Ca	0.0285	n.a.	n.a.	n.a.
	Aq600	Mn/Ca	0.3716	n.a.	n.a.	n.a.
	Aq600	Mn/Ca	0.3716	n.a.	n.a.	n.a.
<i>Aulimina lessonii</i>	All	Mg/Ca	<u><0.0001</u>	<u><0.0001</u>	<u><0.0001</u>	0.4302
	All	S/Ca	<u><0.0001</u>	<u><0.0001</u>	<u><0.0001</u>	0.4657
	All	Na/Ca	0.1227	0.0013	0.0231	<u><0.0001</u>
	Aq10	Mn/Ca	0.0065	n.a.	n.a.	n.a.
	Aq600	Mn/Ca	0.0788	n.a.	n.a.	n.a.
	Aq600	Mn/Ca	0.0788	n.a.	n.a.	n.a.

Bold values are significantly different ($p < 0.05$). Underlined values are conservatively significant after Bonferroni correction, $p_{\text{Bonferroni}} < 0.00086$ ($p_{\text{Bonferroni}} < 0.05/n$, with $n = \text{total number of } t\text{-test} = 58$). Note that for *Bulimina marginata*, no secondary peak and base are analyzed. EPMA, electron probe microanalysis.

seawater [Mn] (**Table 2**). The Mn/Ca values collected by EPMA (semiquantitative method) and LA-ICP-MS (quantitative method) by Barras et al. (2018) are given in **Table 5** and are in agreement for the Aq600 (*Ammonia* sp. and *B. marginata*) and Aq100 (*B. marginata*), but the calibration of EPMA is not sufficient when Mn/Ca is below ~2,500 ppm (value of *Ammonia* sp. in Aq100 and *B. marginata* in Aq10; **Table 5**).

For all species, we observe that with increasing seawater [Mn], Mn/Ca_{EPMA} for both peak and base increases (**Table 5**; **Figure 7**). Even though incorporation of Mn is species specific (Mn/Ca_{EPMA} = *Ammonia* sp. < *B. marginata* < *A. lessonii*), peak intensity is very similar between species (~1.5×).

Distribution of Mg, Mn, and Sr by Nanoscale Secondary Ion Mass Spectrometry

Examples of elemental maps and linescans obtained by nanoSIMS can be found in **Figure 8** and **Supplementary Figure 4**. We investigated the co-occurrence of peak positions of Sr/Ca and Mn/Ca with Mg/Ca (counts/counts) in the linescans ($n = 5$ for *A. lessonii* and $n = 11$ for *B. marginata*) from Aq10, based on the location of the Mg/Ca peaks. For *Ammonia* sp., we obtained too few linescans ($n = 2$) to quantify peak and base values. Results from statistical comparison

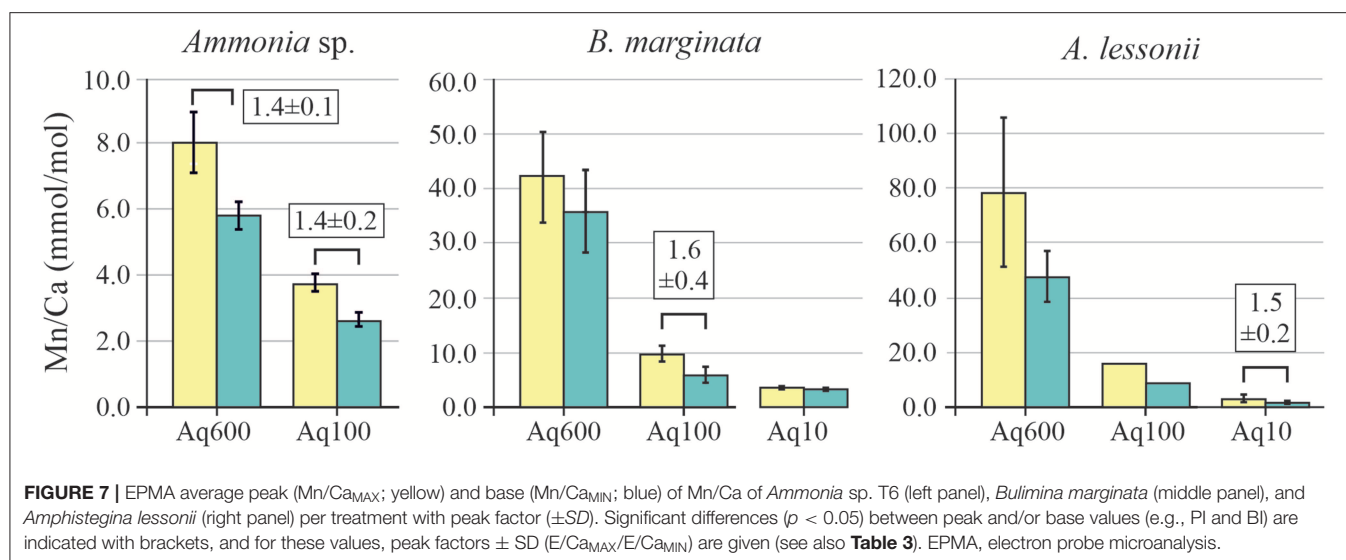


TABLE 5 | Mn/Ca peak (Mn/Ca_{MAX}) and base (Mn/Ca_{MIN}) values for *Ammonia* sp. T6, *Bulimina marginata*, and *Amphistegina lessonii* with peak factor (PF; significant values in bold, see **Table 4**) and average values obtained by EPMA analyses (see **Table 2**).

Species	Aq	n	Avg Mn/Ca _{LA}	Avg Mn/Ca _{EPMA} (mmol/mol)	Peak I Mn/Ca _{MAX}	Base I Mn/Ca _{MIN}	PF (MAX/MIN)
<i>Ammonia</i> sp.	Aq100	3	0.86 ± 0.10	3.1 ± 0.2	3.8 ± 0.3	2.7 ± 0.2	1.4 ± 0.2
	Aq600	5	4.74 ± 0.75	5.5 ± 1.1	8.0 ± 0.9	5.8 ± 0.4	1.4 ± 0.01
<i>B. marginata</i>	Aq10	2	0.67 ± 0.07	3.3 ± 0.1	3.7 ± 0.3	3.4 ± 0.4	1.1 ± 0.3
	Aq100	3	6.16 ± 0.62	9.3 ± 1.0	9.9 ± 1.5	6.3 ± 1.1	1.6 ± 0.4
	Aq600	3	34.3 ± 3.94	33.3 ± 4.3	42.6 ± 9.0	35.8 ± 7.5	1.2 ± 0.01
<i>A. lessonii</i>	Aq10	4	n.a.	3.3 ± 0.1	4.1 ± 0.5	3.0 ± 0.2	1.5 ± 0.2
	Aq100	1	n.a.	13.6 ± 2.2	16.9	9.9	1.7
	Aq600	4	n.a.	65.7 ± 15.5	78.3 ± 27.2	47.8 ± 9.2	1.6 ± 0.3

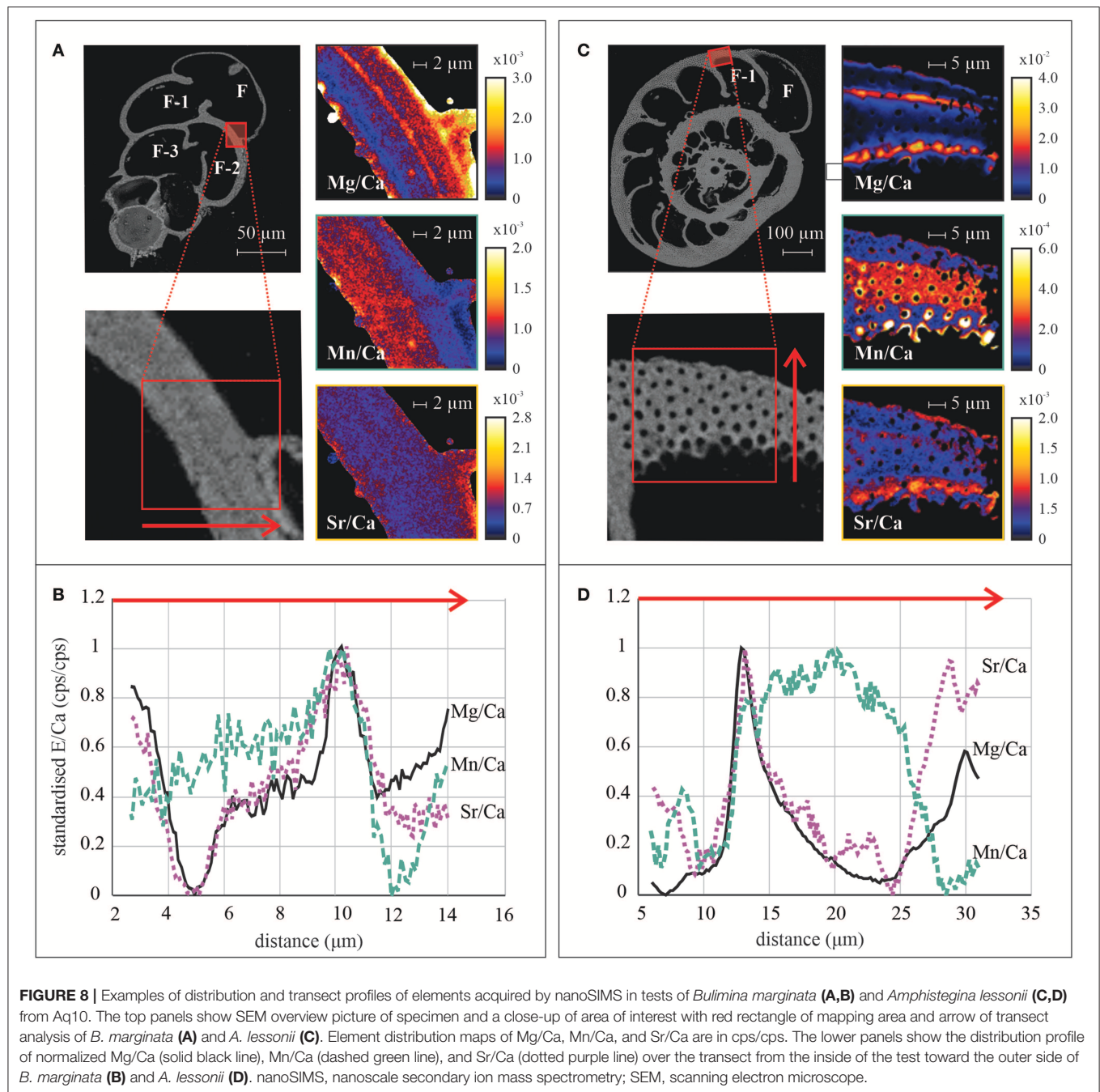
Average Mn/Ca_{LA} (mmol/mol ± SD) is from Barras et al. (2018). n.a., not available; EPMA, electron probe microanalysis.

(*p* values) of averages of peaks and bases for *B. marginata* and *A. lessonii* can be found in **Table 6** and **Figure 9**. In both species, the first Mg peak (PI), associated with the primary layer of calcite, is the most pronounced and significantly higher than the second peak (*p* < 0.0001 and 0.005, respectively, for *B. marginata* and *A. lessonii*; **Table 6**, **Figure 9A**). Based on visual observations, Sr/Ca seems to follow the pattern of Mg/Ca (**Figure 8B** for *B. marginata* and **Figure 8D** for *A. lessonii*). However, only for *B. marginata* did we observe that the first peak (PI) is significantly higher than the second peak (PII; **Figure 9C**), as observed for Mg/Ca. For *A. lessonii*, the difference between the Sr/Ca of PI and PII is not significantly different, maybe owing to the lower sample number (*n* = 5 vs. *n* = 11 for *B. marginata*). In contrast, Mn/Ca distribution is clearly different or offset from Mg/Ca, which is reflected by low normalized peak values with larger SD in both species (**Figure 9B**).

Manganese Speciation by Micro-X-Ray Absorption Near-Edge Structure

The first observations of the combined spectra from the different locations, that is, internal coating (**Figure 10C**) and calcite

locations (**Figure 10D**) with reference spectra, suggests that Mn is systematically under a Mn(II) speciation. The results of the PCA performed on normalized (second derivative) spectra of all samples (in total 169 spectra) plus the set of references (measured during the ID21 synchrotron session and from other authors; Johnson et al., 2016; Blamey et al., 2018) are presented in **Figure 10A**. The first two axes of the PCA explain 77% of the variability of the data. The analysis highlights the clear difference in the chemical environment of Mn between the “internal coating” location and the measurements performed in the calcite itself (“high Mn calcite_{EXP},” “low Mn calcite_{PRE},” and “high Mn calcite_{PRE}”). The averaged spectra for the different locations (all species and aquaria combined, **Figure 10B**) show that the near-edge features are mainly characterized by two distinct peaks in the calcite, whereas only one large white line peak is observed for the “internal coating” zone. Regarding the calcite samples, the spectra are in general following the same trend, but the intensities of the near-edge peaks seem to be variable (**Supplementary Figure 5B**, **Supplementary Table 1**), and the PCA suggests some small differences between the two species and between the two [Mn] conditions, for example, high Mn calcite_{PRE} locations of



Bulimina (Aq100) and *Ammonia* (Aq100) in **Figure 10A** and **Supplementary Figure 5A**.

Some references plot close to the different areas defined by the locations in the samples, that is, calcite samples (“high Mn calcite_{EXP},” “high Mn calcite_{PRE},” and “low Mn calcite_{PRE}”) and internal coating, meaning that their spectra show similar trends as the samples of these areas. In **Figures 10C,D**, the averaged spectra of the samples are presented with the associated references for each location. Internal coating spectra exhibit very similar patterns to several references such as MnSO₄,

MnPO₄ (**Figure 10C**), and Mn-organic compounds published in Blamey et al. (2018), for example, Mn-oxalate, Mn-phytate, and Mn-cystine. The spectra for calcite locations show similar features as kutnohorite (CaMn(CO₃)₂) and manganoan calcite ((Ca,Mn)CO₃) published in Johnson et al. (2016) with a smaller pre-edge peak and two distinct peaks in the near-edge region of the spectra. However, the intensity and sharpness of the peaks are slightly different from the references and also between species and conditions. For example, the intensity of the white line peak of *Bulimina*-Aq600 is higher than that of

TABLE 6 | Two-tailed *p*-values of unpaired *t*-test of comparison of means of primary and secondary peak (PI and PII) and base (BI and BII) values of E/Ca acquired by nanoSIMS.

Species	E/Ca	PI/BI	PII/BII	PI/PII	BI/BII
<i>Bulimina marginata</i>	Mg/Ca	>0.0001	>0.0001	>0.0001	0.9808
	Mn/Ca	0.2180	0.8241	0.5553	0.5363
	Sr/Ca	>0.0001	>0.0001	0.0004	0.1170
<i>Aulimina lessonii</i>	Mg/Ca	>0.0001	>0.0001	0.0005	0.3097
	Mn/Ca	0.9052	0.7254	0.9040	0.5258
	Sr/Ca	0.0026	0.0004	0.7176	0.3352

Bold values are significantly different ($p < 0.05$). Underlined values are conservatively significant after Bonferroni correction, $p_{\text{Bonferroni}} < 0.00086$ ($p_{\text{Bonferroni}} < 0.05/n$, with $n =$ total number of *t*-test = 58). nanoSIMS, nanoscale secondary ion mass spectrometry.

Ammonia-Aq100 (Supplementary Figure 5B), and the energy of white line peaks is different between conditions (Aq600 and Aq100) for each species (Supplementary Figure 5C). Although the calcite Mn/Ca ratio may partly influence the analyses, the normalization of the spectra should reduce this effect. Moreover, the potential bias due to self-adsorption effects, which could change according to different [Mn] in the sample, has been assessed and, in the concentrations of Mn considered here, would not be sufficient to explain the differences observed between the “high Mn calcite_{EXP}” spectra from different species and aquaria (see Supplementary Figure 5 for comparison of the “high Mn calcite_{EXP}” spectra).

For the moment, it is difficult to explain the reason for this discrepancy. On the one hand, we could have variable contributions from an additional Mn phase to the XANES signal observed in calcite, and in this case, we could be missing an appropriate reference that would plot on the negative side of the PC1 axis where all the newly formed calcites are plotting. Considering that the depth resolution of the XRF analyses is $\sim 30 \mu\text{m}$, we are analyzing a depth mixture of different parts of the test, which could include an additional Mn phase. For now, we can, however, suppose that the main signal measured in the calcite corresponds to MnCaCO_3 phase. Considering the references available in this study, we believe that a linear combination would not be reliable, and quantitative analyses would require the preparation and analysis of a wider set of references.

DISCUSSION

Intra-Test Variability of Mg, Na, S, and Sr Distribution of Mg, Na, S, and Sr Follows Laminar Calcification Model

By combining the EPMA and nanoSIMS data, we can summarize the spatial distribution of several elements in three species of foraminifera, that is, *Ammonia* sp. T6, *Bulimina marginata* (which has never been studied before in this context), and *Amphistegina lessonii*. All three species show high a variation of Mn, Mg, Na, S, and Sr in their test while being cultured in a controlled laboratory setup with stable conditions. Therefore, any

heterogeneity is not a function of fluctuation of environmental parameters nor due to migration of the foraminifera in the sediment or water column. To compare the intra-test variation of Mn with that of the other elements, we first need to discuss the banding observed for Mg, Na, S, and Sr. From EPMA and nanoSIMS measurements, we observe a correlation between the locations of high concentration bands of Mg, Na, S, and Sr. The number of high concentration bands, especially the Mg banding, which is the most pronounced, seems to be linked to the investigated position of the chamber, that is, only one high-band in the ultimate chamber and two high-bands in the penultimate chamber. The three species studied follow the laminar calcification model proposed for hyaline foraminifera (for example, see Erez, 2003; Sadekov et al., 2005). During a calcification event (i.e., creation of a new chamber), the chamber is composed of a primary layer of calcite and followed by a secondary layer of calcite that will cover the rest of the test or preexisting chambers (Reiss, 1958; Hemleben et al., 1977, 1986; Bé et al., 1979). The co-occurrence of number of calcite lamella and highly concentrated bands implies that element banding might be intrinsically linked to the laminar calcification in these foraminifera, as suggested before (Erez, 2003; Jonkers et al., 2016; van Dijk et al., 2017b; Geerken et al., 2018). The high concentration bands are located in the first part of each lamella, close to the primary organic sheet, where calcification commences. This is in line with previous studies on small and larger benthic foraminifera showing thin high concentration of these elements close to the location of the organic sheets (Erez, 2003; Paris et al., 2014; van Dijk et al., 2017b, 2019; Geerken et al., 2018, 2019).

The presence of organic material, like organic linings between calcite lamellae, could cause a higher Mg content owing to increased adsorption of Mg (Mavromatis et al., 2017). If that is also the case for other elements, for example, S and Na, this could be the reason behind the observed covariation of banding of Mg and other elements, as suggested earlier by Kunioka et al. (2006) for planktic foraminifera. However, this is disputed by the work of Amiel et al. (1973), Busenberg and Plummer (1985), and Kitano et al. (1975), who show that sulfate and sodium are predominately in solid solution and not a component of the organic matrix of biogenic (Mg-)calcites. Also, the (small) spatial offset observed between the organic layers and the elemental band, as shown previously for *Alobifera gibbosa* (by EPMA; van Dijk et al., 2017b), *Alobifera lobifera* (by electron probe WDS; Erez, 2003), and *Orbulina universa* (by nanoSIMS; Paris et al., 2014), suggests that the banding is not directly related to the organic matter content.

The location of concentrated bands might be explained by a small amount of seawater enclosed in the site of calcification (SOC; de Nooijer et al., 2014) or input of unmodified seawater through small openings in the organic sheet enveloping the SOC, which has been observed at the start of calcification (Nagai et al., 2018). When it was assumed that foraminiferal calcification occurs in a closed system, the Rayleigh fractionation, as proposed by Elderfield et al. (1996), fails to explain the observed banding at the start of the lamellae. Indeed, higher E/Ca is expected to be observed when Ca is being utilized (Evans et al., 2018),

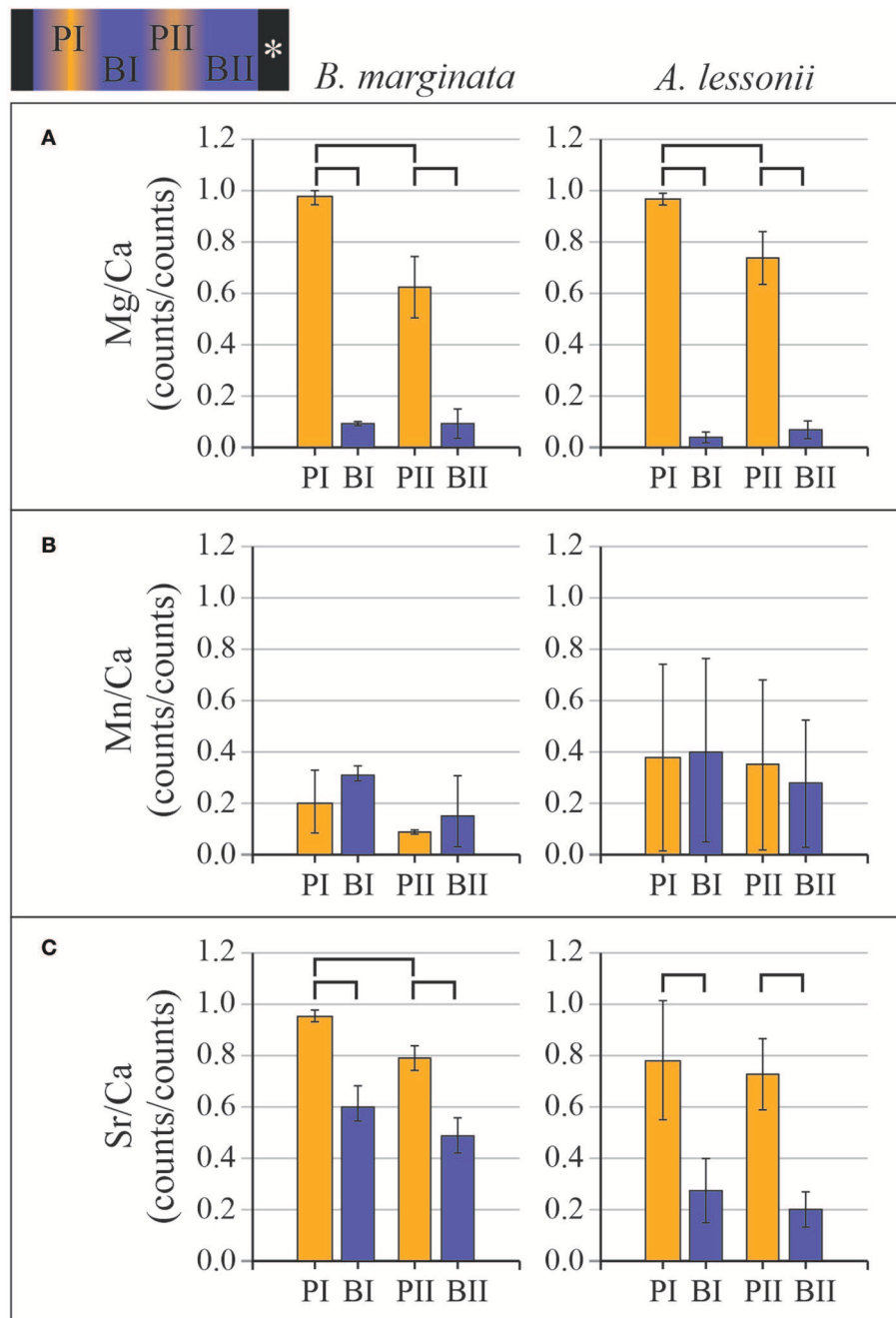


FIGURE 9 | Normalized average values of primary peak and base (PI and BI) and secondary peak and base (PII and BII) for the two species *Bulimina marginata* (left panels) and *Ammonia lessonii* (right panels) from Aq10 for **(A)** Mg/Ca, **(B)** Sr/Ca, and **(C)** Mn/Ca derived from profiles obtained by nanoSIMS analysis (for example, see **Figure 8**). The top shows a hypothetical transect map with locations of PI, BI, PII, and BII, with the asterisk indicating the outer part of the test. Note that peak-base data are in counts/counts, unlike semiquantitative EPMA data presented in **Figures 6, 7**. nanoSIMS, nanoscale secondary ion mass spectrometry; EPMA, electron probe microanalysis.

which would lead to higher E/Ca on the external part of the lamella. Following the trans-membrane transport mixing model (Nehrke et al., 2013; Mewes et al., 2014), banding can be explained by import of Ca^{2+} in the SOC during calcification. This would “dilute” the E/Ca at the SOC, leading to a lower

E/Ca in the rest of the lamellae. The reasons for differences in elements incorporation between species (**Table 2**, this study; van Dijk et al., 2017a) are partially unknown but have been hypothesized to be caused by different contributions of processes involved in biomineralization responsible for element uptake

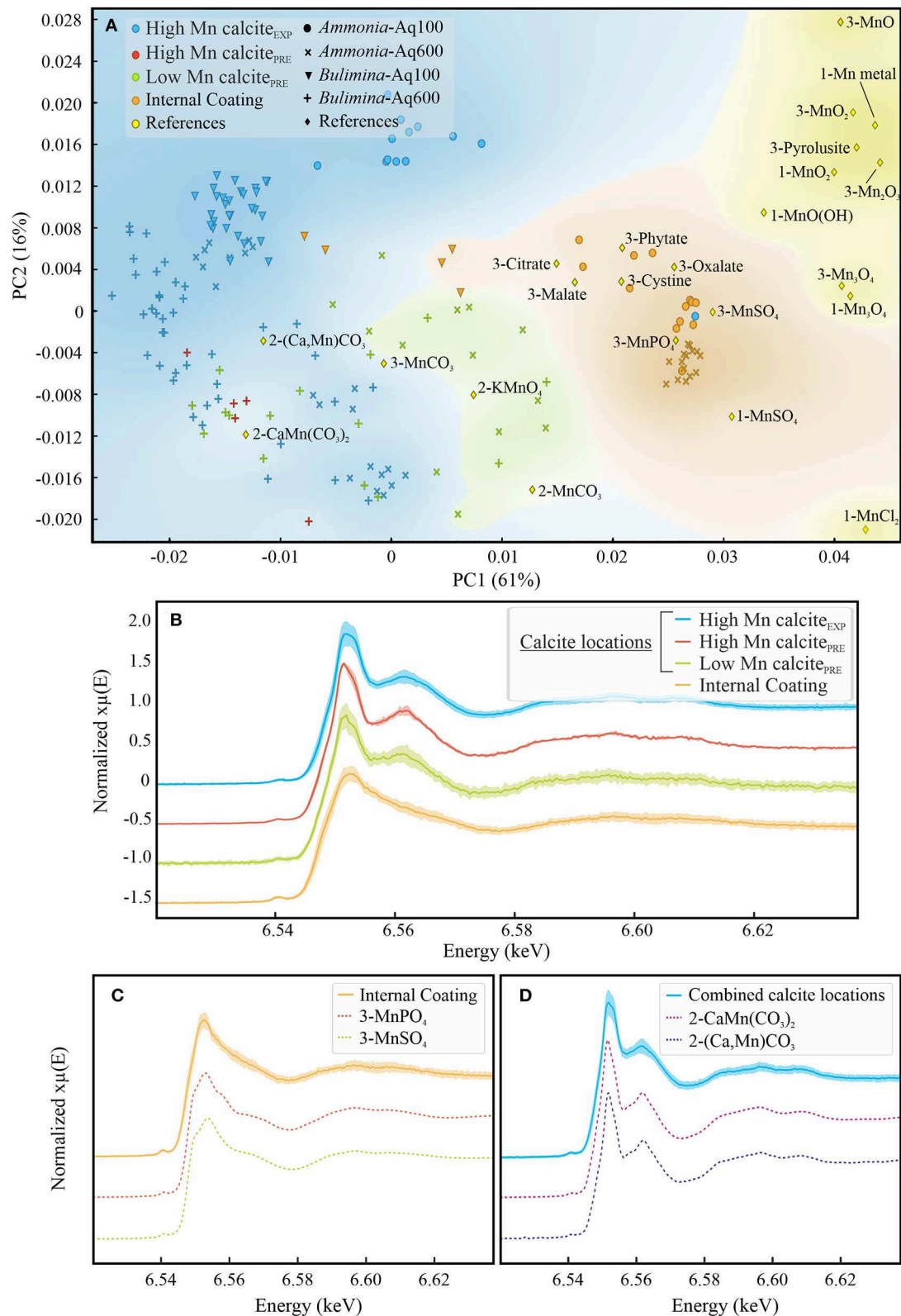


FIGURE 10 | Summary of μ XANES analyses. PCAs performed on all normalized (second derivative) spectra (both species, both aquaria, and all locations) and on reference spectra **(A)**. Average spectra \pm SD for the different locations ("high Mn calcite_{EXP}," "high Mn calcite_{PRE}," "low Mn calcite_{PRE}," and "internal coating"; **B**). The average spectra \pm SD of **(C)** "internal coating" and **(D)** calcite locations (i.e., "high Mn calcite_{EXP}," "high Mn calcite_{PRE}," and "low Mn calcite_{PRE}" spectra combined), plotted with spectra of the reference material. Please note that for panels **(B–D)**, a shift has been applied on the y-axis to improve readability. μ XANES, micro-X-ray absorption near-edge structure; PCA, principal component analysis.

(Mewes et al., 2014). For example, variable passive transport and Ca^{2+} pumping efficiency could result in different element incorporation between species (Nehrke et al., 2013; Geerken et al., 2018) and might also explain our observed differences in peak intensity (Figure 6, Table 3). Banding is most intense for Mg, which is tightly biologically controlled (Zeebe and Sanyal, 2002; Bentov and Erez, 2006; de Nooijer et al., 2014). If changes in transport, uptake, or incorporation of Mg during chamber formation are responsible for Mg banding, the incorporation of Mg might lead to higher incorporation of other elements, like Na and Sr, owing to crystal lattice strain.

Differences in Banding Intensity of Mg, Na, and S Between Species

Although banding can be explained by the incorporation of elements that is, over time, diluted as a result of pumping of Ca^{2+} in the SOC, the difference in the absolute values of E/Ca between the low Mg species *Ammonia* sp. and *B. marginata* and the intermediate Mg species *A. lessonii* (Table 2) might be explained by the abundance of seawater endocytosis, as suggested before to explain the chemical fingerprint of S and Mg in a wide range of foraminiferal species (van Dijk et al., 2019). Vacuoles of seawater have been observed in *A. lessonii* (e.g., Bentov et al., 2009) but are so far not resolved in *Ammonia* sp. or *B. marginata*. In fact, according to the observations of Nehrke et al. (2013), they would play only a minor role in the calcification of *Ammonia* sp. The seawater in these vacuoles is altered by various pumps and possible channels, like $\text{Ca}^{2+}/\text{H}^{+}$ and $\text{Na}^{+}/\text{H}^{+}$ channels, to increase internal pH and [Ca] (Erez, 2003), and Mg/Ca of this calcification fluid is lowered to ~ 2 mol/mol (Evans et al., 2018). Seawater vacuoles, high in Ca, represent still a considerable flux of Mg but are low in Na ions owing to the proposed pumps. The chemical signature of the vacuoles (low [Na], but still relatively high [Mg]) could explain why tests of *A. lessonii* have a $5\times$ higher Mg/Ca than have tests of *Ammonia* sp. and *B. marginata*, whereas Na/Ca is only $\sim 1.5\times$ higher. Another explanation is offered by Geerken et al. (2019), who hypothesized that Na and Sr banding is higher for *A. lessonii* compared with *Ammonia* sp. owing to crystal lattice strain, allowing for higher incorporation of alkali elements, like Sr, owing to lattice distortion (Mucci and Morse, 1983). Even though it is not certain if Na is affected by lattice strain, because this element is incorporated interstitially (Ishikawa and Ichikuni, 1984), it fits the observations by Evans et al. (2015), who showed that foraminiferal Na/Ca increases with Mg/Ca.

Species *B. marginata* has slightly higher average test Mg/Ca than has *Ammonia* sp. (Table 2), but both species have similar base values for Mg/Ca (Figure 6 and Mg, Na, and S Distribution: Electron Probe Microanalysis Peak Analysis section). These results suggest that the difference in total test Mg/Ca between these species is caused by the higher peak value. This higher E/Ca in the banding of *B. marginata* could be caused by either a larger volume of seawater enclosed at the SOC, as suggested by de Nooijer et al. (2014), or more passive transport of seawater at the start of calcification, when the protective envelop is not completely closed (Nagai et al., 2018). The first theory, not directly proven yet, could be revealed by analyzing

calcification fluid in the SOC by, for example, cryo-SEM, or cryo-nanoSIMS, which would allow for the measurement of fully hydrated samples. Furthermore, the evolution of the protective organic sheet enclosing the SOC has so far only been studied on *Ammonia* (Nagai et al., 2018) and will need to be studied for other species to investigate its link to intra-test variability in E/Ca. Interestingly, for Na/Ca, peak and base values increase from *Ammonia* sp. and *B. marginata* to *A. lessonii* (Figure 6B), suggesting that sodium content in these species is determined by both peak and base values, and not just the peak intensity, as suggested for Mg/Ca and S/Ca (van Dijk et al., 2019). As a monovalent ion, Na^{+} , compared with Mg^{2+} , would be incorporated at the same time but perhaps differently to the crystal lattice.

Element Banding in Foraminiferal Calcite Due To Vital Effects: Synthesis

In Table 7, we show an overview of all data on element banding in foraminiferal tests currently available, including our observations. We included only studies investigating “internal” banding, in the primary and secondary layers of calcite, and we excluded studies focusing on crust formation (e.g., Eggins et al., 2003; Sadekov et al., 2009; Marr et al., 2013; Steinhart et al., 2015) or studies that do not discuss mechanistic responsible for banding (Sadekov et al., 2010; Vetter et al., 2013). We conclude that all bandings reported in this table are due to vital effects, that is, due to processes active during chamber formation, like biomineralization processes. However, not one mechanism alone can explain all observations for both benthic and planktic species, suggesting that there might be a combination of factors causing and modulating banding of elements in foraminifera. For both planktic and benthic foraminifera, the hypothesis that Mg banding in the calcite would correspond to organic linings enrichments between calcite lamellae (Erez, 2003; Kunioka et al., 2006) does not allow to explain the co-occurrence of Na and S banding that is predominately in solid solution and not a component of the organic matrix in a range of biogenic calcites (Amiel et al., 1973; Kitano et al., 1975; Busenberg and Plummer, 1985). For foraminifera, the coordination of Mg and B is uniform across the banding of individual tests, rebutting a double-phase Mg incorporation (Branson et al., 2013, 2015). Furthermore, *Ammonia* sp. has a relatively thick organic lining than have other species (Ni Fhlaithearta et al., 2013), which would, hypothetically, lead to a more pronounced organic signal in the banding. However, this is in contrast to our results and other studies (Geerken et al., 2018, 2019; van Dijk et al., 2019), which all show that banding intensity is low for *Ammonia* sp. compared with other species, like *Amphistegina*. Lastly, most often, banding in tests from both benthic and planktonic species is found adjacent to and not directly on the organic linings (Hathorne et al., 2009; van Dijk et al., 2017b). On the basis of this combined evidence, we conclude that the banding observed in foraminiferal calcite is not likely to be caused by the presence of organic matter in the test wall.

For planktonic foraminifera with and without symbionts, day–night cycling is suggested to be responsible for the observed banding, whether by processes involved in biomineralization

TABLE 7 | Overview of planktonic and benthic species with heterogeneous element distribution in the chamber wall, including proposed mechanisms responsible for banding.

Species	Element	Mechanisms responsible
PLANKTONIC SPECIES WITH SYMBIONTS		
<i>Orbulina universa</i>	Mg	Symbiont-associated pH changes (Eggins et al., 2004; Sadekov et al., 2005) Changes in mitochondrial density/activity (Spero et al., 2015) Processes involved in biomineralization (Sadekov et al., 2005)
<i>Globigerinoides ruber</i>	Mg	Biomineralization processes and/or algal symbionts activity (Sadekov et al., 2005; Fehrenbacher and Martin, 2014)
<i>Pulleniatina obliquiloculata</i>	Mg, Sr	Laminar calcification model/organic linings (Kunioka et al., 2006)
PLANKTONIC SPECIES WITHOUT SYMBIONTS		
<i>Neogloboquadrina dutertrei</i>	Mg	Biomineralization processes (Fehrenbacher et al., 2017) Changes in calcification temperature due to migration (Sadekov et al., 2005)
<i>Neogloboquadrina incompta</i>	Mg	Changes in calcification temperature due to migration (Sadekov et al., 2005)
<i>Globorotalia menardii</i>		
<i>Globorotalia truncatulinoides</i>		
<i>Neogloboquadrina pachyderma</i>	Mg	Chamber formation processes (Jonkers et al., 2016)
<i>Globorotalia inflata</i>	Mg	Not due to calcite precipitation rate, Rayleigh distillation of the calcifying reservoir, and organic linings (Hathorne et al., 2009)
<i>Globorotalia scitula</i>		
BENTHIC SPECIES WITH SYMBIONTS		
<i>Alobifera lobifera</i>	Mg, S	Laminar calcification model/organic linings (Erez, 2003)
<i>Amphistegina lessonii</i>	Mg, Na, S, Sr	Chamber addition/biomineralization processes; Ca-pumping (This study; Geerken et al., 2018)
	Mn	Symbiont activity; oxygenation of microenvironment (this study)
	B	Biomineralization processes: change in internal pH or ion transport (Branson et al., 2015)
BENTHIC SPECIES WITHOUT SYMBIONTS		
<i>Ammonia</i> sp.	Mg, Na, S, Sr	Chamber addition/biomineralization processes; Ca-pumping (This study; Geerken et al., 2018, 2019; van Dijk et al., 2019)
	Mn	Chamber addition/biomineralization processes; Ca-pumping (this study)
<i>Bulimina marginata</i>	Mg, Na, S, Sr	Chamber addition/biomineralization processes; Ca-pumping (this study)
	Mn	Variable Ca-pumping/passive transport, or chamber 3D structure, compared with <i>Ammonia</i> sp. (this study)
<i>Uvigerina peregrina</i>	Mg	Laminar calcification model (Glock et al., 2012)
<i>Bolivina spissa</i>	Mg banding absent	Chamber 3D structure: monolamellar calcification model (Glock et al., 2012)

(Fehrenbacher et al., 2017) or changes in the activity and density of mitochondria during chamber formation (Spero et al., 2015). Changes in pH of the microenvironment due to symbiont activity, proposed by Eggins et al. (2004) and Sadekov et al. (2005), might modulate the banding but cannot explain its occurrence, because Mg banding is also present in non-symbiont species (Fehrenbacher et al., 2017).

Benthic foraminifera, especially deep-sea species like *B. marginata*, should not be sensitive to day–night cycling, and banding is more likely to be the result of processes involved in chamber additions, like unmodified seawater at the SOC (de Nooijer et al., 2014) by, for example, openings in the organic sheet at the start of calcification (Nagai et al., 2018) and consequently “dilution” of E/Ca of the SOC owing to Ca-proton pumping (Nehrke et al., 2013; Toyofuku et al., 2017). It is likely that banding in benthic foraminifera is tightly coupled to chamber addition and the lamellar calcification model. The lack of Mg banding observed for *Bolivina spissa* is explained by Glock et al. (2012) with the fact that this species has a monolamellar

calcification structure (Sliter, 1974). However, even with a monolamellar species, one would still expect elemental banding in lamellae of older chambers. The lack of Mg banding observed for this species by Glock et al. (2012) might be due to other reasons, maybe related to, for example, calcification processes in *B. spissa*, or low intensity of the Mg and the sensitivity of the method used.

Variability of Mn Speciation and Distribution in Foraminiferal Test Walls
Coordination of Mn in *Ammonia* sp. and *B. marginata*
 For the first time, we demonstrate that Mn is also heterogeneously distributed in the test wall of the three investigated species (**Figure 5**). On the basis of our results, we observed no clear difference of coordination of Mn throughout the test wall, suggesting that this element might be present in a unique chemical phase throughout the test wall, as also observed by XANES for Mg and B in the test wall of *A. lessonii* (Branson et al., 2013, 2015). Considering the set of Mn

reference materials, Mn phase(s) present in the calcite mostly resembles the coordination of Mn in kutnohorite ($\text{CaMn}(\text{CO}_3)_2$) or manganoan calcite ($(\text{Ca,Mn})\text{CO}_3$) with a well-organized structure compared with that of more amorphous organic references. These results seem to confirm that Mn^{2+} ions are mainly present in octahedral coordination geometry and that a large part of Mn^{2+} substitutes Ca^{2+} in the carbonate matrix during the process of biomineralization. However, the spectra from calcite locations do not fit perfectly with any carbonate references, leading to the idea that there could be a contribution of other Mn phases, with proportions that would slightly change according to species and/or seawater [Mn] (or Mn/Ca ratio in the calcite). For example, De Giudici et al. (2018) found that Zn is mainly substituted for Ca in calcite of benthic foraminifera sampled in a heavy metal-polluted area, but detectable amounts can also be found as hydrozincite, a carbonate phase that would be the result of biological processes. It is possible that the variability observed in μXANES spectra acquired in the calcite is the result of a slightly different contribution of several Mn phases or bias due to depth resolution of the analyses. To overcome this problem, future work should focus on thin sections, which would avoid mixing the signals in depth but, on the other hand, would reduce the sensitivity for certain elements.

Finally, measurements by μXRF were not able to detect changes between low and high Mn bands inside the calcite, but we did observe in some cases a coating on the inside of the foraminiferal test and within the pores (Figure 4B). This coating is enriched in Mn and shows a patchy distribution. μXANES spectra from these areas are very different from the spectra acquired in the calcite layers and present the same features as the organic references analyzed. To our opinion, this coating would correspond to the remaining cytoplasm enriched in Mn (e.g., Mn associated with organic compounds), even though specimens were cleaned with NaOCl . This highlights the importance of the organic removal step, because especially in the case of bulk analyses, the remaining cytoplasm of such an enriched Mn coating would result in artificially higher foraminiferal Mn/Ca values.

Microdistribution of Mn in Foraminiferal Calcite

Even though the coordination of Mn seems to be relatively similar within and between specimens of *Ammonia* sp. and *B. marginata*, the distribution patterns of Mn are, however, very different for the three species studied here and are comparable with the distribution of Mg, Na, S, and Sr (e.g., Figure 5). Peak intensity is similar (e.g., significant peak factors in Figure 7; Table 4), but the distribution patterns and peak location of Mn/Ca differ for the three species, which might be due to the characteristics of Mn ions (e.g., ion radius), in combination with chamber structure, potentially Mn-rich coatings, and symbiont activity. For *Ammonia* sp., the distribution of Mn/Ca follows variations of Mg/Ca, with thin banding located at the start of the lamella (Figure 5 and Supplementary Figure 1). This suggests that Mn follows similar pathways as the other elements, like Mg. For this species, the theoretical model of Mn adsorption layers proposed by Barras et al. (2018) to explain their ontogenetic trends in Mn/Ca could fit. This model

would involve Mn-enriched phase (adsorbed Mn ions) between secondary calcite that could superimpose with increased Mn bands linked to biomineralization processes (cf. explanations for Mg incorporation) between lamella.

The adsorption model by Barras et al. (2018) cannot fully explain the observed distribution of Mn in tests of *B. marginata* and *A. lessonii*. Mn incorporation in *A. lessonii* might be influenced by activity of symbionts, because symbionts perform photosynthesis during the light cycle that increases the oxygen concentration and pH in the foraminiferal microenvironment (Köhler-Rink and Köhl, 2000, 2001). If the kinetics of Mn oxidation/reduction is faster than 12 h, the production of oxygen and pH change could cause a change in the speciation of manganese near the foraminifera, lowering free Mn^{2+} due to the oxidation of Mn^{2+} to Mn^{3+} , which has a strong affinity for natural organic ligands (Oldham et al., 2017). Although it is not possible in our data to distinguish between day and night calcites, a clear difference can be observed between Mn/Ca values of different lamella in almost all of our maps. Because it is not logical that Mn partitioning changes for different calcification events, the amount of free Mn^{2+} in the foraminiferal microenvironment might be modified by symbiont activity (Köhler-Rink and Köhl, 2005; Glas et al., 2012). Symbiont activity, linked to the day–night cycle, might determine the average value of the lamella. A small number of maps of *A. lessonii* do not show contrasting Mn/Ca for different lamella (e.g., Supplementary Figure 3B, middle panel), which were likely precipitated both during day. For these maps, we observe a Mn distribution similar to that of *Ammonia* sp., which might be linked to a Mn adsorption phase discussed earlier. Further investigation is needed to couple day–night cycle to the foraminiferal calcite, by, for example, spiking experiments, in which an isotope spike is added to the culture media during day or nighttime.

Because *B. marginata* is a small benthic low-Mg species like *Ammonia* sp., we could expect to observe similar features in the distribution of elements. Although this is the case for Mg, S, and Sr, the microdistribution of Mn in *B. marginata* is quite different and even highly variable between specimens. Mn/Ca and Mg/Ca are often negatively correlated with or high concentration bands of these elements being spatially offset (Figure 5 and Supplementary Figure 2B). Therefore, it is much more difficult to explain the different patterns observed for this species, also because it has not been studied before in terms of element microdistribution. This anticorrelation could suggest a competition of Mn and other elements in the crystal lattice. However, we do not observe this for *Ammonia* sp., which has E/Ca values in the same order of magnitude. The species *B. marginata* is incorporating much higher quantities of Mn in their test; the Mn/Ca is six times higher than that of *Ammonia* sp. (in Aq600) while these species are grown in the same culture setup (Barras et al., 2018). Higher incorporation of Mn in the species *B. marginata* could be explained by (i) more additional Mn through seawater vacuolization, or (ii) less selective pumping of Ca^{2+} channels/pumps, leading to the accidental transport of Mn^{2+} , or (iii) species-specific differences in internal pH, leading to changes in the speciation of Mn. The presence of seawater vacuoles has not been studied in this species. Because the radius

of the Mn^{2+} ion is very close to that of Ca^{2+} , the second explanation might be plausible but not proven. Nevertheless, the three hypotheses do not explain the observed distribution pattern in the test wall. We can only speculate that the (bio)availability, transport, or uptake of Mn during chamber formation, which can be influenced by pH (Zachara et al., 1991) and oxygen level (Reichert et al., 2003; Tribovillard et al., 2006), might be different for *B. marginata* compared with *Ammonia* sp. The differences in a Mn distribution of different species (Figure 5 and Supplementary Figure 2) could then perhaps be explained by a difference in pH and/or oxygenation during chamber formation.

Implications for Proxy Development and Biomineralization Models

For the benthic species investigated here, almost all of the observed banding patterns of Mg/Ca, Na/Ca, S/Ca, and Sr/Ca seem to be coupled to laminar calcification model (as defined by Reiss, 1957). This has to be taken into account when creating calibrations based on LA-ICP-MS data, because an artificial offset can be created between proxy calibration and application by measuring different chambers that include different proportions of high and low concentration areas. In contrast, the distribution of redox-sensitive element Mn is less straightforward, showing high variability between and, in the case of *B. marginata*, within species (Supplementary Figures 1–4). Other redox-sensitive elements should be investigated on the microscale level to conclude if this is potentially coupled to pH or oxygenation of the foraminiferal microenvironment or in the SOC during chamber addition. The increased partitioning observed for Mn in *B. marginata*, D_{Mn} of 0.621, compared with *Ammonia* sp., D_{Mn} of 0.086 (Barras et al., 2018), could be explained by the observed increased Mn incorporation during test thickening in tests of *B. marginata*, as shown by EPMA (e.g., Supplementary Figure 2). Nevertheless, the overall Mn/Ca value still follows seawater [Mn] (Table 2), which is in agreement with Barras et al. (2018). Bulk analyses can, therefore, still be used to reconstruct seawater [Mn] and ultimately redox conditions/oxygen level. However, on the basis of the spatial heterogeneity observed with EPMA and nanoSIMS, we would underline the need for multiple measurements on multiple specimens, if possible, to gain a robust understanding of the average test E/Ca. Especially when investigating distribution of elements in the foraminiferal test, this is crucial, because the patterns of certain elements are highly variable between specimens (see Supplementary Figures 1–3 for examples).

CONCLUSIONS

Through a combination of EPMA and nanoSIMS and synchrotron microanalyses, we investigated the distribution of multiple elements and speciation of Mn in three species of benthic foraminifera—small symbiont-barren species *Ammonia* sp. T6 and *Bulimina marginata* and larger symbiont-bearing species *Amphistegina lessonii*—cultured in controlled laboratory conditions. Distribution patterns of Mg, Na, S, and Sr in chamber walls of benthic foraminifera seem to be coupled

to lamellae developed during chamber formation, showing thin concentrated bands at the start of the lamellae and lower values toward the exterior. In contrast, the distribution of redox-sensitive element Mn is less straightforward, showing high variability between species. Mn seems to mainly substitute Ca in the crystal lattice according to the μXANES analyses performed on *Ammonia* sp. and *B. marginata*. For *Ammonia* sp., Mn/Ca follows the same pattern as the other investigated elements. For the species *A. lessonii*, we observed thick high and low Mn banding, corresponding to different lamellae, which might be caused by photosymbiotic activity. The day–night cycle of the symbionts could affect the oxygen level in the microenvironment of the foraminifera, leading to a shift in the available Mn during these periods. A Mn distribution in tests of *B. marginata* compared with *Ammonia* sp. shows high variability and often a spatial offset or anticorrelation with Mg, leading to higher average Mn/Ca. We are currently not able to fully explain the observed variation of Mn in *B. marginata*. Our study, based on a multielement distribution and different species, highlights the complexity of biomineralization processes in benthic foraminifera and the potential uncertainty in trace elemental-based paleoceanographic reconstructions.

DATA AVAILABILITY STATEMENT

The datasets generated for this study are available on request to the corresponding author.

AUTHOR CONTRIBUTIONS

SO, AM, and CB planned and performed the culture experiment. ID, AM, and CB performed the measurements and analyzed the results. HF, SL, G-JR, JR-H, and MC facilitated the technical realization of the study. The manuscript was written under the leadership of ID. All authors contributed to the discussion and interpretation of the results.

FUNDING

This research was funded by University Bretagne Loire and Angers Loire Metropole (project MOXY by CB) and the French national program EC2CO-LEFE (project MANGA 2D by AM). The ESRF is thanked for granting beam time at ID21 (ES-682). JR-H acknowledges the Mexican National Council for Science and Technology (CONACYT) for the funding of his post-doctoral position (CONACYT CVU#177448). Further financial support comes from the Netherlands Earth System Science Center (NESSC; Grant No. 024.002.001 by G-JR). HF acknowledges funding from the Swedish Research Council VR (Grant No. 2017-04190).

ACKNOWLEDGMENTS

We would like to thank Olivier Teisserenc for developing oxygen control system (including PYTHON script) used to maintain stable oxygen concentrations during the culture experiment and

Romain Mallet from the SCIAM platform at Angers University for his help with SEM pictures. Great thanks to Tilly Bouten and Sergei Matveev for technical support with the EPMA. Prof. Anders Meibom and Dr. Stephane Escrig are thanked for access to the nanoSIMS instrument in the Laboratory for Biological Geochemistry at EPFL and for help with data acquisition and data analysis. Wout de Nolf is thanked for his support during the experiment at ID21. Lastly, we would like to thank Samuel

M. Webb and Peter Kopittke for providing manganese reference spectra for μ XANES.

SUPPLEMENTARY MATERIAL

The Supplementary Material for this article can be found online at: <https://www.frontiersin.org/articles/10.3389/feart.2019.00281/full#supplementary-material>

REFERENCES

- Allison, N., Finch, A. A., Sutton, S. R., and Newville, M. (2001). Strontium heterogeneity and speciation in coral aragonite: implications for the strontium paleothermometer. *Geochim. Cosmochim. Acta* 65, 2669–2676. doi: 10.1016/S0016-7037(01)00628-7
- Amiel, A. J., Friedman, G. M., and Miller, D. S. (1973). Distribution and nature of incorporation of trace elements in modern aragonitic corals. *Sedimentology* 20, 47–64. doi: 10.1111/j.1365-3091.1973.tb01606.x
- Barras, C., Mouret, A., Nardelli, M. P., Metzger, E., Petersen, J., La, H. L., et al. (2018). Experimental calibration of manganese incorporation in foraminiferal calcite. *Geochim. Cosmochim. Acta* 237, 49–64. doi: 10.1016/j.gca.2018.06.009
- Bé, A. W. H., Hemleben, C., Anderson, O. R., and Spindler, M. (1979). Chamber formation in planktonic foraminifera. *Micropaleontology* 25, 294–307. doi: 10.2307/1485304
- Bentov, S., Brownlee, C., and Erez, J. (2009). The role of seawater endocytosis in the biomineralization process in calcareous foraminifera. *Proc. Natl. Acad. Sci. U.S.A.* 106, 21500–21504. doi: 10.1073/pnas.0906636106
- Bentov, S., and Erez, J. (2006). Impact of biomineralization processes on the Mg content of foraminiferal shells: a biological perspective. *Geochim. Geophys. Geosyst.* 7:Q01P08. doi: 10.1029/2005GC001015
- Bernhard, J. M., Blanks, J. K., Hintz, C. J., and Chandler, G. (2004). Use of the fluorescent calcite marker calcein to label foraminiferal tests. *J. Foraminiferal Res.* 34, 96–101. doi: 10.2113/0340096
- Blamey, F. P. C., McKenna, B. A., Li, C., Cheng, M., Tang, C., Jiang, H., et al. (2018). Manganese distribution and speciation help to explain the effects of silicate and phosphate on manganese toxicity in four crop species. *New Phytol.* 217, 1146–1160. doi: 10.1111/nph.14878
- Branson, O., Kaczmarek, K., Redfern, S. A. T., Misra, S., Langer, G., Tyliczszak T., et al. (2015). The coordination and distribution of B in foraminiferal calcite. *Earth Planet. Sci. Lett.* 416, 67–72. doi: 10.1016/j.epsl.2015.02.006
- Branson, O., Redfern, S. A., Tyliczszak, T., Sadekov, A., Langer, G., Kimton, et al. (2013). The coordination of Mg in foraminiferal calcite. *Earth Planet. Sci. Lett.* 383, 134–141. doi: 10.1016/j.epsl.2013.09.037
- Busenberg, E., and Plummer, N. L. (1985). Kinetic and thermodynamic factors controlling the distribution of SO_4^{2-} and Na^+ in calcites and selected aragonites. *Geochim. Cosmochim. Acta* 49, 713–725. doi: 10.1016/0016-7037(85)90166-8
- Cotte, M., Fabris, T., Agostini, G., Motta Meira, D., De Viguier, L., Solé, V., et al. (2016). Watching kinetic studies as chemical maps using open-source software. *Anal. Chem.* 88, 6154–6160. doi: 10.1021/acs.analchem.5b04819
- Cotte, M., Pouyet, E., Salomé, M., Rivard, C., De Nolf, W., Castillo-Michel, H., et al. (2017). The ID21 X-ray and infrared microscopy beamline at the ESRF: status and recent applications to artistic materials. *J. Anal. At. Spectrom.* 32, 477–493. doi: 10.1039/C6JA00356G
- De Giudici, G., Meneghini, C., Medas, D., Buosi, C., Zuddas, P., Iadecola, A., et al. (2018). Coordination environment of Zn in foraminifera *Elphidium aculeatum* and *Quinqueloculina seminula* shells from a polluted site. *J. Chem. Geol.* 477, 100–111. doi: 10.1016/j.chemgeo.2017.12.009
- de Nooijer, L. J., Spero, H. J., Erez, J., Bijma, J., and Reichart, G.-J. (2014). Biomineralization in perforate foraminifera. *Earth-Sci. Rev.* 135, 48–58. doi: 10.1016/j.earscirev.2014.03.013
- Demšar, J., Curk, T., Erjavec, A., Gorup, C., Hočevar, T., Milutinovič, M., et al. (2013). Orange: data mining toolbox in python. *Python. J. Mach. Learn. Res.* 14, 2349–2353.
- Eggins, S., de Deckker, P., and Marshall, J. (2003). Mg/Ca variation in planktonic foraminifera tests: implications for reconstructing palaeo-seawater temperature and habitat migration. *Earth Planet. Sci. Lett.* 212, 291–306. doi: 10.1016/S0012-821X(03)00283-8
- Eggins, S., Sadekov, A., and Dedecker, P. (2004). Modulation and daily banding of Mg/Ca in tests by symbiont photosynthesis and respiration: a complication for seawater thermometry? *Earth Planet. Sci. Lett.* 225, 411–419. doi: 10.1016/j.epsl.2004.06.019
- Elderfield, H., Bertram, C. J., and Erez, J. (1996). A biomineralization model for the incorporation of trace elements into foraminiferal calcium carbonate. *Earth Planetary Sci. Lett.* 142, 409–423. doi: 10.1016/0012-821X(96)00105-7
- Elderfield, H., Vautravers, M., and Cooper, M. (2002). The relationship between shell size and Mg/Ca, Sr/Ca, $\delta^{18}\text{O}$, and $\delta^{13}\text{C}$ of species of planktonic foraminifera. *Geochim. Geophys. Geosyst.* 3, 1–13. doi: 10.1029/2001GC000194
- Erez, J. (2003). The source of ions for biomineralization in foraminifera and their implications for paleoceanographic proxies. *Rev. Mineral. Geochem.* 54, 115–149. doi: 10.2113/0540115
- Evans, D., Erez, J., Oron, S., and Müller, W. (2015). Mg/Ca-temperature and seawater-test chemistry relationships in the shallow-dwelling large benthic foraminifera *Operculina ammonoides*. *Geochim. Cosmochim. Acta* 148, 325–342. doi: 10.1016/j.gca.2014.09.039
- Evans, D., and Müller, W. (2013). LA-ICP-MS elemental imaging of complex discontinuous carbonates: an example using large benthic foraminifera. *J. Anal. At. Spectrom.* 28, 1039–1044. doi: 10.1039/c3ja50053e
- Evans, D., Müller, W., and Erez, J. (2018). Assessing foraminifera biomineralisation models through trace element data of cultures under variable seawater chemistry. *Geochim. Cosmochim. Acta* 236, 198–217. doi: 10.1016/j.gca.2018.02.048
- Fehrenbacher, J. S., and Martin, P. A. (2014). Exploring the dissolution effect on the intrashell Mg/Ca variability of the planktic foraminifer *Globigerinoides ruber*. 29, 854–868. doi: 10.1002/2013PA002571
- Fehrenbacher, J. S., Russell, A. D., Davis, C. V., Gagnon, A., Spero, H. J., Cliff, J. B., et al. (2017). Link between light-triggered Mg-banding and chamber formation in the planktic foraminifera *Neogloboquadrina dutertrei*. *Nat. Commun.* 8:15441. doi: 10.1038/ncomms15441
- Fehrenbacher, J. S., Spero, H. J., Russell, A. D., Vetter, L., Eggins, S., et al. (2015). Optimizing LA-ICP-MS analytical procedures for elemental depth profiling of foraminifera shells. *Chem. Geol.* 407–408, 2–9. doi: 10.1016/j.chemgeo.2015.04.007
- Freitas, P. S., Clarke, L. J., Kennedy, H., and Richardson, C. A. (2009). Ion microprobe assessment of the heterogeneity of Mg/Ca, Sr/Ca, and Mn/Ca ratios in *Pecten maximus* and *Mytilus edulis* (bivalvia) shell calcite precipitated at constant temperature. *Biogeosciences* 6, 1209–1227. doi: 10.5194/bg-6-1209-2009
- Fujita, K., Okai, T., and Hosono, T. (2014). Oxygen metabolic responses of three species of large benthic foraminifera with algal symbionts to temperature stress. *PLoS ONE* 9:e90304. doi: 10.1371/journal.pone.0090304
- Geerken, E., de Nooijer, L. J., Roepert, A., Polerecky, L., King, H. E., and Reichart, G. J. (2019). Element banding and organic linings within chamber walls of two benthic foraminifera. *Sci. Rep.* 9:3598. doi: 10.1038/s41598-019-40298-y
- Geerken, E., de Nooijer, L. J., van Dijk, I., and Reichart, G. J. (2018). Impact of salinity on element incorporation in two benthic foraminiferal species with contrasting magnesium contents. *Biogeosciences* 15, 2205–2218. doi: 10.5194/bg-15-2205-2018

- Glas, M. S., Fabricius, K. E., de Beer, D., and Uthicke, S. (2012). The O_2 , pH and Ca^{2+} microenvironment of benthic foraminifera in a high CO_2 world. *PLoS ONE* 7:e50010. doi: 10.1371/journal.pone.0050010
- Glock, N., Liebetrau, V., Vogts, A., and Eisenhauer, A. (2019). Organic heterogeneities in foraminiferal calcite traced through the distribution of N, S, and I measured with nanoSIMS: a new challenge for element-ratio-based paleoproxies? 7:175. doi: 10.3389/feart.2019.00175
- Glock, N., Eisenhauer, A., Liebetrau, V., Wiedenbeck, M., Hensen, C., and Nehrke, G. (2012). EMP and SIMS studies on Mn/Ca and Fe/Ca systematics in benthic foraminifera from the Peruvian OMZ: a contribution to the identification of potential redox proxies and the impact of cleaning protocols. *Biogeosciences* 9, 341–359. doi: 10.5194/bg-9-341-2012
- Groeneveld, J., and Filipsson, H. L. (2013). Mg/Ca and Mn/Ca ratios in benthic foraminifera: the potential to reconstruct past variations in temperature and hypoxia in shelf regions. *Biogeosciences* 10, 5125–5138. doi: 10.5194/bg-10-5125-2013
- Groeneveld, J., Filipsson, H. L., Austin, W. E., N. Darling, K., McCarthy, D., Quintana Krupinski, N. B., et al. (2018). Assessing proxy signatures of temperature, salinity, and hypoxia in the Baltic Sea through foraminifera-based geochemistry and faunal assemblages. *J. Micropalaeontol.* 37, 403–429. doi: 10.5194/jm-37-403-2018
- Guo, X., Xu, B., Burnett, W. C., Yu, Z., Yang, S., Huang, X., et al. (2019). A potential proxy for seasonal hypoxia: LA-ICP-MS Mn/Ca ratios in benthic foraminifera from the Yangtze River Estuary. *Geochim. Cosmochim. Acta* 245, 290–303. doi: 10.1016/j.gca.2018.11.007
- Hathorne, E. C., James, R. H., and Lampitt, R. S. (2009). Environmental versus biomineralization controls on the intratest variation in the trace element composition of the planktonic foraminifera *G. inflata* and *G. scitula*. *Paleoceanography* 24:PA4204. doi: 10.1029/2009PA001742
- Hemleben, C., Be, A. W. H., Anderson, O. R., and Tuntivate, S. (1977). Test morphology, organic layers and chamber formation of the planktonic foraminifer *Globorotalia menardii* (d'Orbigny). *J. Foraminiferal Res.* 7, 1–25. doi: 10.2113/gsjfr.7.1.1
- Hemleben, C. H., Anderson, O. R., Berthold, W., and Spindler, M. (1986). "Calcification and chamber formation in Foraminifera—a brief overview," in *Biomineralization in Lower Plants and Animals*, eds B. S. Leadbeater and R. Riding (Oxford: Clarendon Press), 237–249.
- Hintz, C. J., Shaw, T. J., Bernhard, J. M., Chandler, G., McCorkle, D. C., and Blanks, J. K. (2006). Trace/minor element:calcium ratios in cultured benthic foraminifera. Part II: Ontogenetic variation. *Geochim. Cosmochim. Acta* 70, 1964–1976. doi: 10.1016/j.gca.2005.12.019
- Hönisch, B., and Hemming, N. G. (2005). Surface ocean pH response to variations in pCO_2 through two full glacial cycles. *Earth Planetary Sci. Lett.* 236, 305–314. doi: 10.1016/j.epsl.2005.04.027
- Hoppe, P., Cohen, S., and Meibom, A. (2013). NanoSIMS: technical aspects and applications in cosmochemistry and biological geochemistry. *Geostand. Geoanal. Res.* 37, 111–154. doi: 10.1111/j.1751-908X.2013.00239.x
- Ishikawa, M., and Ichikuni, M. (1984). Uptake of sodium and potassium by calcite. *Chem. Geol.* 42, 137–146. doi: 10.1016/0009-2541(84)90010-X
- Johnson, J. E., Webb, S. M., Ma, C., and Fischer, W. W. (2016). Manganese mineralogy and diagenesis in the sedimentary rock record. *Geochim. Cosmochim. Acta* 173, 210–231. doi: 10.1016/j.gca.2015.10.027
- Jonkers, L. Buse, B. G., Brummer, J. A., and Hall, I. R. (2016). Chamber formation leads to Mg/Ca banding in the planktonic foraminifer *Neogloboquadrina pachyderma*. *Earth Planet. Sci. Lett.* 451, 177–184. doi: 10.1016/j.epsl.2016.07.030
- Kitano, Y., Okumura, M., and Idogaki, M. (1975). Incorporation of sodium, chloride and sulfate with calcium carbonate. *Geochem. J.* 9, 75–84. doi: 10.2343/geochemj.9.75
- Köhler-Rink, S., and Kühl, M. (2001). Microsensor studies of photosynthesis and respiration in the larger symbiont bearing foraminifera *Amphistegina lobifera*, and *Amphisorus hemprichii*. *Ophelia* 55, 111–122. doi: 10.1080/00785236.2001.10409478
- Köhler-Rink, S., and Kühl, M. J. (2000). Microsensor studies of photosynthesis and respiration in larger symbiotic foraminifera. I The physico-chemical microenvironment of *Marginopora vertebralis*, *Amphistegina lobifera* and *Amphisorus hemprichii*. *Mar. Biol.* 137, 473–486. doi: 10.1007/s00227000335
- Köhler-Rink, S., and Kühl, M. J. (2005). The chemical microenvironment of the symbiotic planktonic foraminifer *Orbulina universa*. *Mar. Biol. Res.* 1, 68–78. doi: 10.1080/17451000510019015
- Koho, K. A., de Nooijer, L. J., and Reichart, G. J. (2015). Combining benthic foraminiferal ecology and shell Mn/Ca to deconvolve past bottom water oxygenation and paleoproductivity. *Geochim. Cosmochim. Acta* 165, 294–306. doi: 10.1016/j.gca.2015.06.003
- Kunioka, D., Shirai, K., Takahata, N., Sano, Y., Toyofuku, T., and Ujiie, Y. (2006). Microdistribution of Mg/Ca, Sr/Ca, and Ba/Ca ratios in *Pulleniatina obliquiloculata* test by using a NanoSIMS: implication for the vital effect mechanism. *Geochem. Geophys. Geosyst.* 7:Q12P20. doi: 10.1029/2006GC001280
- Lear, C. H., Elderfield, H., and Wilson, P. A. (2000). Cenozoic deep-sea temperatures and global ice volumes from Mg/Ca in benthic foraminiferal calcite. *Science* 287, 269–272. doi: 10.1126/science.287.5451.269
- Marr, J. P., Bostock, H. C., Carter, L. Bolton, A., and Smith, E. (2013). Differential effects of cleaning procedures on the trace element chemistry of planktonic foraminifera. *Chem. Geol.* 351, 310–323. doi: 10.1016/j.chemgeo.2013.05.019
- Mavromatis, V., Immenhauser, A., Buhl, D., Purgstaller, B., Baldermann, A., and Dietzel, M. (2017). Effect of organic ligands on Mg partitioning and Mg isotope fractionation during low-temperature precipitation of calcite in the absence of growth rate effects. *Geochim. Cosmochim. Acta* 207, 139–153. doi: 10.1016/j.gca.2017.03.020
- McKay, C. L., Groeneveld, J., Filipsson, H. L., Gallego-Torres, D., Whitehouse, M., and Romero, O. E. (2015). A comparison of benthic foraminiferal Mn/Ca and sedimentary Mn/Al as proxies of relative bottom-water oxygenation in the low-latitude NE Atlantic upwelling system. *Biogeosciences* 12, 5415–5428. doi: 10.5194/bg-12-5415-2015
- Mewes, A., Langer, G., de Nooijer, L. J., Bijma, J., and Reichart, G. (2014). Effect of different seawater Mg^{2+} concentrations on calcification in two benthic foraminifers. *Mar. Micropaleontol.* 113, 56–64. doi: 10.1016/j.marmicro.2014.09.003
- Mucci, A., and Morse, J. W. (1983). The incorporation of Mg^{2+} and Sr^{2+} into calcite overgrowths: influences of growth rate and solution composition. *Geochim. Cosmochim. Acta* 47, 217–233. doi: 10.1016/0016-7037(83)90135-7
- Nagai, Y., Uematsu, K., Chen, C., Wani, R., Tyska, J., and Toyofuku, T. (2018). Weaving of biomineralization framework in rotaliid foraminifera: implications for paleoceanographic proxies. *Biogeosciences* 15, 6773–6789. doi: 10.5194/bg-15-6773-2018
- Nehrke, G., Keul, N., Langer, G., de Nooijer, L. J., Bijma, J., and Meibom, A. (2013). A new model for biomineralization and trace - element signatures of Foraminifera tests. *Biogeosciences* 10, 6759–6767. doi: 10.5194/bg-10-6759-2013
- Ní Fhlaithearta, S., Ernst, S. R., Nierop, K. G., de Lange, G., and Reichart, G.-J. (2013). Molecular and isotopic composition of foraminiferal organic linings. *Mar. Micropaleontol.* 102, 69–78. doi: 10.1016/j.marmicro.2013.06.004
- Ní Fhlaithearta, S., Fontanier, C., Jorissen, F., Mouret, A., Dueñas-Bohórquez, A., Anschutz, P., et al. (2018). Manganese incorporation in living (stained) benthic foraminiferal shells: a bathymetric and in-sediment study in the Gulf of Lions (NW Mediterranean). *Biogeosciences* 15, 6315–6328. doi: 10.5194/bg-15-6315-2018
- Nürnberg, D., Bijma, J., and Hemleben, C. (1996). Assessing the reliability of magnesium in foraminiferal calcite as a proxy for water mass temperatures. *Geochim. Cosmochim. Acta* 60, 803–814. doi: 10.1016/0016-7037(95)00446-7
- Oldham, V. E., Mucci, A., Tebo, B. M., and Luther, G. W. III. (2017). Soluble Mn(III)–L complexes are abundant in oxygenated waters and stabilized by humic ligands. *Geochim. Cosmochim. Acta* 199, 238–246. doi: 10.1016/j.gca.2016.11.043
- Paris, G., Fehrenbacher, J. S., Sessions, A. L., Spero, H., and Adkins, J. F. (2014). Experimental determination of carbonate-associated sulfate $\delta^{34}S$ in planktonic foraminifera shells. *Geochem. Geophys. Geosyst.* 15, 1452–1461. doi: 10.1002/2014GC005295
- Petersen, J., Barras, C., Bézos, A., La, C., de Nooijer, L. J., Meysman, F. J. R., et al. (2018). Mn/Ca intra- and inter-test variability in the benthic foraminifer *Ammonia tepida*. *Biogeosciences* 15, 331–348. doi: 10.5194/bg-15-331-2018
- Ravel, B., and Newville, M. (2005). ATHENA, ARTEMIS, HEPHAESTUS: data analysis for X-ray absorption spectroscopy using IFEFFIT. *J. Synchrotron Radiat.* 12, 537–541. doi: 10.1107/S0909049505012719

- Reeder, R. J., Lamble, G. M., and Northrup, P. A. (1999). XAFS study of the coordination and local relaxation around Co^{2+} , Zn^{2+} , Pb^{2+} , and Ba^{2+} trace elements in calcite. *Am. Mineral.* 84, 1049–1060. doi: 10.2138/am-1999-7-807
- Reichart, G.-J., Jorissen, F., Anschutz, P., and Mason, P. R. (2003). Single foraminiferal test chemistry records the marine environment. *Geology* 31, 355–358. doi: 10.1130/0091-7613(2003)031<0355:SFTCRT>2.0.CO;2
- Reiss, Z. (1957). The Bilamellidea, nov. superfam., and remarks on cretaceous globorotaliids. *Contrib. Cushman Found. Foraminiferal Res.* 8, 127–145.
- Reiss, Z. (1958). Classification of lamellar foraminifera. *Micropaleontology* 4, 51–70. doi: 10.2307/1484251
- Richirt, J., Schweizer, M., Bouchet, V. M. P., Mouret, A., Quinchard, S., and Jorissen, F. J. (2019). Morphological distinction of three ammonia phylotypes occurring along european coasts. *J. Foraminiferal Res.* 49, 76–93. doi: 10.2113/gsjfr.49.1.76
- Sadekov, A., Eggins, S. M., De Deckker, P., and Kroon, D. (2008). Uncertainties in seawater thermometry deriving from intratest and intertest Mg/Ca variability in *Globigerinoides ruber*. *Paleoceanography* 23:PA1215. doi: 10.1029/2007PA001452
- Sadekov, A., Eggins, S. M., De Deckker, P., Ninnemann, U., Kuhnt, W., and Bassinot, F. (2009). Surface and subsurface seawater temperature reconstruction using Mg/Ca microanalysis of planktonic foraminifera *Globigerinoides ruber*, *Globigerinoides sacculifer*, and *Pulleniatina obliquiloculata*. *Paleoceanogr. Paleoclimat.* 24:PA3201. doi: 10.1029/2008PA001664
- Sadekov, A. Y., Eggins, S. M., and de Deckker, P. (2005). Characterization of Mg/Ca distributions in planktonic foraminifera species by electron microprobe mapping. *Geochem. Geophys. Geosyst.* 6:Q07012. doi: 10.1029/2005GC000973
- Sadekov, A. Y., Eggins, S. M., Klinkhammer, G. P., and Rosenthal, Y. (2010). Effects of seafloor and laboratory dissolution on the Mg/Ca composition of *Globigerinoides sacculifer* and *Orbulina universa* tests — A laser ablation ICPMS microanalysis perspective. *Earth Planet. Sci. Lett.* 292, 312–324. doi: 10.1016/j.epsl.2010.01.039
- Sano, Y., Shirai, K., Takahata, N., Hirata, T., and Sturchio, N. C. (2005). Nano-SIMS analysis of Mg, Sr, Ba and U in natural calcium carbonate. *Anal. Sci.* 21, 1091–1097. doi: 10.2116/analsci.21.1091
- Sliter, W. V. (1974). Test ultrastructure of some living benthic foraminifers. *Lethaia* 7, 5–16. doi: 10.1111/j.1502-3931.1974.tb00880.x
- Solé, V. A., Papillon, E., Cotte, M., Walter, P., and Susini, J. (2007). A multiplatform code for the analysis of energy-dispersive X-ray fluorescence spectra. *Spectrochim. Acta B Atom. Spectrosc.* 62, 63–68. doi: 10.1016/j.sab.2006.12.002
- Spero, H. J., Eggins, S. M., Russell, A. D., Vetter, L., Kilburn, M. R., and Hönisch, B. (2015). Timing and mechanism for intratest Mg/Ca variability in a living planktic foraminifer. *Earth Planet. Sci. Lett.* 409, 32–42. doi: 10.1016/j.epsl.2014.10.030
- Steinhardt, J., de Nooijer, L. L. J., Brummer, G.-J., and Reichart, G.-J. (2015). Profiling planktonic foraminiferal crust formation. *Geochem. Geophys. Geosyst.* 16, 2409–2430. doi: 10.1002/2015GC005752
- Sulu-Gambari, F., Seitaj, D., Behrends, T., Banerjee, D., Meysman, F. J., and Slomp, C. P. (2016). Impact of cable bacteria on sedimentary iron and manganese dynamics in a seasonally-hypoxic marine basin. *Geochim. Cosmochim. Acta* 192, 49–69. doi: 10.1016/j.gca.2016.07.028
- Toplak, M., Birarda, G., Read, S., Sandt, C., Rosendahl, S. M., Vaccari, L., et al. (2017). Infrared orange: connecting hyperspectral data with machine learning. *Synchrotron Radiat. News* 30, 40–45. doi: 10.1080/08940886.2017.1338424
- Toyofuku, T., Matsuo, M. Y., de Nooijer, L. J., Nagai, Y., Kawada, S., Fujita, K., et al. (2017). Proton pumping accompanies calcification in foraminifera. *Nat. Commun.* 8:14145. doi: 10.1038/ncomms14145
- Tribouillard, N., Algeo, T. J., Lyons, T., and Riboulleau, A. (2006). Trace metals as paleoredox and paleoproductivity proxies: an update. *Chem. Geol.* 232, 12–32. doi: 10.1016/j.chemgeo.2006.02.012
- Urey, H. C., Lowenstam, H. A., Epstein, S., and McKinney, C. R. (1951). Measurement of paleotemperatures and temperatures of the upper Cretaceous of England, Denmark and the southeastern United States. *GSA Bull.* 62, 399–416. doi: 10.1130/0016-7606(1951)62[399:MOPATO]2.0.CO;2
- van Dijk, I., Barras, C., de Nooijer, L. J., Mouret, A., Geerken, E., Oron, S., et al. (2019). Coupled calcium and inorganic carbon uptake suggested by magnesium and sulfur incorporation in foraminiferal calcite. *Biogeosciences* 16, 2115–2130. doi: 10.5194/bg-16-2115-2019
- van Dijk, I., de Nooijer, L. J., Boer, W., and Reichart, G. J. (2017b). Sulfur in foraminiferal calcite as a potential proxy for seawater carbonate ion concentration. *Earth Planet. Sci. Lett.* 470, 64–72. doi: 10.1016/j.epsl.2017.04.031
- van Dijk, I., de Nooijer, L. J., and Reichart, G. J. (2017a). Trends in element incorporation in hyaline and porcelaneous foraminifera as a function of $p\text{CO}_2$. *Biogeosciences* 14, 497–510. doi: 10.5194/bg-14-497-2017
- Vetter, L., Spero, H. J., Russell, A. D., and Fehrenbacher, J. (2013). LA-ICP-MS depth profiling perspective on cleaning protocols for elemental analyses in planktic foraminifers. *Geochem. Geophys. Geosyst.* 14, 2916–2931. doi: 10.1002/ggge.20163
- Weiner, S., and Dove, P. M. (2003). An overview of biomineralization processes and the problem of the vital effect. *Rev. Mineral. Geochem.* 54, 1–29. doi: 10.1515/9781501509346-006
- Wu, G., and Hillaire-Marcel, C. (1995). Application of LP-ICP-MS to benthic foraminifers. *Geochim. Cosmochim. Acta* 59, 409–414. doi: 10.1016/0016-7037(94)00370-2
- Zachara, J. M., Cowan, C. E., and Resch, C. T. (1991). Sorption of divalent metals on calcite. *Geochim. Cosmochim. Acta* 55, 1549–1562. doi: 10.1016/0016-7037(91)90127-Q
- Zeebe, R. E., Bijma, J., Honisch, B., Sanyal, A., Spero, H. J., and Wolf-Gladrow, D. A. (2008). Vital effects and beyond: a modelling perspective on developing palaeoceanographical proxy relationships in foraminifera. *Geol. Soc. London Special Publ.* 303, 45–58. doi: 10.1144/SP303.4
- Zeebe, R. E., and Sanyal, A. (2002). Comparison of two potential strategies of planktonic foraminifera for house building: Mg^{2+} or H^+ removal? *Geochim. Cosmochim. Acta* 66, 1159–1169. doi: 10.1016/S0016-7037(01)00852-3

Conflict of Interest: The authors declare that the research was conducted in the absence of any commercial or financial relationships that could be construed as a potential conflict of interest.

Copyright © 2019 van Dijk, Mouret, Cotte, Le Houedec, Oron, Reichart, Reyes-Herrera, Filipsson and Barras. This is an open-access article distributed under the terms of the Creative Commons Attribution License (CC BY). The use, distribution or reproduction in other forums is permitted, provided the original author(s) and the copyright owner(s) are credited and that the original publication in this journal is cited, in accordance with accepted academic practice. No use, distribution or reproduction is permitted which does not comply with these terms.